IEEE Access
Multidisciplinary | Rapid Review | Open Access Journal

Received June 17, 2019, accepted June 29, 2019, date of publication July 4, 2019, date of current version August 1, 2019.

Digital Object Identifier 10.1109/ACCESS.2019.2926717

Microwave Characterization of Low-Loss FDM 3-D Printed ABS With Dielectric-Filled Metal-Pipe Rectangular Waveguide Spectroscopy

JINGYE SUN[1], ATTIQUE DAWOOD[1], WILLIAM J. OTTER[1], NICK M. RIDLER[2], (Fellow, IEEE), AND STEPAN LUCYSZYN[1], (Fellow, IEEE)

[1]Department of Electrical and Electronic Engineering, Imperial College London, London SW7 2AZ, U.K.
[2]Engineering, Materials and Electrical Science Department, National Physical Laboratory, Teddington TW11 0LW, U.K.

Corresponding author: Stepan Lucyszyn (s.lucyszyn@imperial.ac.uk)

This work was supported in part by the Imperial College MRC Confidence in Concept Fund, NIHR Imperial BRC Funding 2015/2016, in part by the U.K.'s Engineering and Physical Sciences Research Council under Grant EP/E063500/1, and in part by the U.K. Space Agency under Grant NSTP3-FT-046.

ABSTRACT Over time, the accuracy and speed by which a material can be characterized should improve. Today, the Nicolson–Ross–Weir (NRW) methodology represents a well-established method for extracting complex dielectric properties at microwave frequencies, with the use of a modern vector network analyzer. However, as will be seen, this approach suffers from three fundamental limitations to accuracy. Challenging NRW methods requires a methodical and robust investigation. To this end, using a dielectric-filled metal-pipe rectangular waveguide, five independent approaches are employed to accurately characterize the sample at the Fabry–Pérot resonance frequency (non-frequency dispersive modeling). In addition, manual *Graphical* and automated *Renormalization* spectroscopic approaches are introduced for the first time in the waveguide. The results from these various modeling strategies are then compared and contrasted to NRW approaches. As a timely exemplar, 3-D printed acrylonitrile–butadiene–styrene (ABS) samples are characterized and the results are compared with existing data available in the open literature. It is found that the various Fabry–Pérot resonance model results all agree with one another and validate the two new spectroscopic approaches; in doing so, exposing three limitations of the NRW methods. It is also shown that extracted dielectric properties for ABS differ from previously reported results and reasons for this are discussed. From measurement noise resilience analysis, a methodology is presented for determining the upper bound signal-to-noise ratio for the vector network analyzer (not normally associated with such instrumentation). Finally, fused deposition modeling (FDM) 3-D printing can result in a non-homogeneous sample that excites open-box mode resonances. This phenomenon is investigated for the first time analytically and with various modeling strategies.

INDEX TERMS 3-D printing, additive manufacturing, ABS, Fabry–Pérot resonance, FDM, open-box mode resonance, MPRWG, NRW, rectangular waveguide, SNR, spectroscopy, VNA.

I. INTRODUCTION

The accurate characterization of a material's complex dielectric properties is of fundamental importance to both the experimental scientist and design engineer. Spectroscopy quantifies the interaction between matter and electromagnetic radiation at discrete frequency points within the spectral range of interest. The authors recently published a comprehensive analytical review paper on the extraction of complex dielectric properties from reflection-transmission mode spectroscopy using free-space (quasi-)optics [1], to try and bridge the knowledge gap between the science and microwave/millimeter-wave/THz engineering communities. In [1], a new graphical-based technique was introduced (in theory only) that avoids the need for: (i) assuming a lossless material; (ii) not considering all Fabry-Pérot reflections between boundaries; and (iii) requiring an initial guess with iterations. As with all previous methods, a number of

The associate editor coordinating the review of this manuscript and approving it for publication was Boxue Du.

generally accepted analytical assumptions were adopted, corresponding to an ideal measurement scenario; associated with the dielectric under test and its measurement environment [1]. However, while this new Graphical technique demonstrated its ability to completely recover (with 100% reliability) the exact complex dielectric properties from an arbitrarily chosen dataset (typical clear window glass, from 1 to 100 THz), using mathematically traceable simulations, until now it has not been applied to real practical (i.e., non-ideal) measurements. Moreover, while spectroscopy is commonly associated with free-space (quasi-)optical measurements, our Graphical technique for extracting complex dielectric properties from reflection-transmission mode spectroscopy will be employed here for the dominant waveguide mode associated with Electronic Industries Alliance (EIA) standard WR-90 (8.2 to 12.4 GHz) for X-band metal-pipe rectangular waveguides (MPRWGs).

Additive manufacturing using polymer-based 3-D printing has received considerable attention in recent years at microwave [2], [3], millimeter-wave [2] and terahertz [4], [5] frequencies. One of the many benefits of this technology is that it offers considerable cost savings over conventional forms of manufacturing; especially with low volume production (e.g., prototyping). However, relatively little has been published on the dielectric properties of these building materials. Moreover, it is generally believed that polymer-based building materials are electromagnetically lossy and, as a result, would not serve as a useful dielectric medium.

The authors recently reported a tunable phase shifter, based on X-band MPRWGs having a mechanically moveable dielectric flap insert; with all parts being 3-D printed [3]. Using simple '*brute-force*' modeling of the dielectric, it was found that the measured relative phase shift tuning performance could be predicted, with the worst-case insertion loss kept below 0.5 dB at 10 GHz; contradicting expectations from previously published dielectric properties for a chemically similar building material.

This paper investigates the characterization of the most commonly found fused deposition modeling (FDM) 3-D printed acrylonitrile-butadiene-styrene (ABS) building material. Not only does this work represent the first practical proof-of-principle demonstration for our new dielectric characterization methodology, but also extends this from relatively simple free-space (quasi-)optics to more complicated waveguide media.

The Graphical approach is fundamentally based on the manual extraction (by visual inspection) of the solution to a set of simultaneous equations. While accurate, it is a very slow and tedious process, which has to be performed at each frequency independently. As a result, a fast automated Renormalization approach is presented here for the first time. These spectroscopic techniques will be independently validated at Fabry-Pérot resonance frequencies. All results will be compared with NRW approaches, using closed-form numerical solutions, which provide a useful benchmark.

It will be rigorously shown that the relatively low loss nature of FDM 3-D printed ABS, found with our initial *brute-force* modeling approach, is validated by various independent approaches; extending its functionality from being just a building material to a useful low loss dielectric medium.

Challenging any well-established approach requires a detailed and rigorous investigation. Improving the current attainable levels of accuracy when characterizing a material's complex dielectric properties raises many complicated and subtle issues. As a result, in this paper, all interrelated aspects will be explored in depth and, in many cases, for the first time. Therefore, in addition to complex dielectric property extraction (the main focus of this paper), supporting insight is given on: (i) 3-D printed sample preparation (which include defects); (ii) modeling of the guided-wave medium containing a sample under test (resulting in the expected Fabry-Pérot mode resonance and unexpected anomalous open-box mode resonances that result from sample defects); (iii) the measurements themselves (which include noise); and (iv) exposing three fundamental limitations to accuracy found with the well-established approach.

Section II details the preparation and quality of the samples and also the measurement set-up that was used; this information is later used by the various characterization methodologies adopted throughout the paper. Section III explores five non-spectroscopic strategies for modeling dielectric-filled metal-pipe rectangular waveguide measurements at the Fabry-Pérot resonance frequency. First, the most accurate analytical method (labeled M1) is employed; from which results from all other methods are compared against. Then much simpler textbook approximations (underpinning many measurement system calibrations, simulation software and complex dielectric property extraction techniques) are given (M2), along with new derivations. These analytical (both accurate and approximate) mathematical models are referred to throughout the paper, to explain background concepts and in performing calculations. Next, a distributed-element equivalent-circuit modeling approach (M3) is given to demonstrate its use in brute-force extraction of dielectric properties using commercial software (underpinned by approximate mathematical models). A lumped-element equivalent-circuit modeling approach (M4) is also included, with new derivations, for modal analysis used later on. Finally, a rigorous (finite-element) numerical electromagnetic simulation software approach (M5) provides an alternative, independent means of extracting the dielectric properties of the samples. All five models (M1 to M5) are used to determine the quality factors associated with the Fabry-Pérot mode. These quality factors provide a useful inter-comparison tool, for validation purposes. Moreover, collectively, all five models give a deep insight into dielectric-filled metal-pipe rectangular waveguides (including the measurements) that are used to house the FDM 3-D printed ABS samples.

Section IV extends the analytical and numerical modeling approaches described in Section III. Bespoke analytical

models are derived to investigate the constituent quality factor contributions associated with the propagating-wave Fabry-Pérot mode resonance, using electromagnetic field integrals calculated either using purely analytical expressions for the electric and magnetic field components or alternatively computed directly from numerical simulations. Section V investigates the standing-wave open-box mode resonances, excited by the imperfections/inhomogeneity in the FDM 3-D printed ABS samples, using numerical techniques discussed in Sections III and IV.

The spectroscopic extraction of complex dielectric properties using the new manual 'Graphical' and the new automated 'Renormalization' approaches are presented in Section VI and Section VII, respectively. In Section VIII, results from these new spectroscopic methodologies are then compared with those extracted using the well-established spectroscopic technique and three non-spectroscopic strategies undertaken at the Fabry-Pérot resonance frequency, as well as those published in the open literature. Section IX investigates the resilience of the well-established and new spectroscopic methodologies to white Gaussian noise found in many real measurement systems. Finally, from the extracted complex dielectric properties of the FDM 3-D printed ABS samples, its use as a practical microwave dielectric is explored and compared with other 3-D printed polymers.

Three appendices are also included in the paper, which provide detailed derivations, analysis and insight into some of the core investigations undertaken within the main body of the paper. Appendix A derives the field integrals needed for quality factor modeling of the Fabry-Pérot resonance modes, covered in Section IV. Appendix B demonstrates how to excite open-box modes using numerical electromagnetic simulation methods, identification of the open-box modes using an eigenmode solver to plot the field patterns, and both analytical and equivalent-circuit modeling approaches to characterize the open-box modes, in support of Section V. Finally, Appendix C presents a new method for determining the upper-bound signal-to-noise power ratio for the frequency-domain vector network analyzer, based on the definition used by space-domain spectrometers, in support of Section IX.

II. SAMPLE PREPARATION AND MEASUREMENTS

A. SAMPLE PREPARATION

Today, FDM 3-D printing is widespread, and possibly set to become ubiquitous within the near future, due to its versatility, ease of use and extremely low cost prints [2]. For this technology, the most common type of amorphous solid thermoplastic building material is the ABS terpolymer (polymer synthesized from three different monomers). The main disadvantages of this low-cost technology are the limitations in minimum feature size and relatively large surface roughness for frequency applications above X-band [2]. It was previously found, with FDM 3-D printed ABS, that the relatively poor layer deposition resolution and relatively poor nozzle positioning repeatability cause significant levels of surface roughness (observed relative peak values were ± 13 μm) and steps (observed relative values were ± 3 μm), respectively [2]. Nevertheless, this entry-level technology was used to demonstrate the manufacture of high performance X-band MPRWG components [2], [3] using the low cost, entry-level desktop 3-D printer (Makerbot Replicator 2X – having a 400 μm nozzle diameter, 100 μm layer resolution with 2.5 μm z-positioning precision, and 11 μm x-y positioning precision).

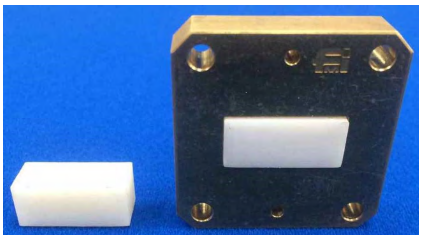

FIGURE 1. Photograph of two FDM 3-D printed ABS samples under test; (left) standalone sample insert; and (right) sample *in-situ* within the nominally air-filled quarter-wavelength thru line section of MPRWG.

Due to current limitations of low-cost entry-level 3-D printing (e.g., poor quality control of the raw-processed building materials, mechanical precision-resolution of the printers and variability of the temperature-speed-infill settings), no two prints will be identical. Moreover, due to the inherent porous nature of FDM 3-D printed structures (allowing an ingress of moisture) and the building material itself (high-energy ultra-violet photons from solar irradiation break the polymer chains), there will be a drift in the complex dielectric properties over time, which depends on the intensity and length of exposure to humidity, sunlight and other environmental factors. To minimize possible discrepancies, with the work presented here, the same reel of ABS filament was used (Formfutura B.V. (Netherlands) 1.75 mm filament diameter Premium ABS - Frosty White – having high impact resistance, reduced warping, good thermal stability and excellent flow behavior [6]). Moreover, our microwave components and dielectric samples were printed from the same printer [3]. Indeed, both sample printing and measurements were performed within two days.

FIGURE 1 shows a photograph of two FDM 3-D printed ABS samples under test, having target dimensions of $22.860 \times 10.160 \times 9.626$ mm^3, with one shown *in-situ* filling a nominally air-filled quarter-wavelength thru line MPRWG. In practice, the x, y and z-dimension have respective ranges of 22.66-22.85 mm, 9.72-10.10 mm and 9.18-9.93 mm.

FIGURE 2 shows photomicrographs of one of the test samples, printed with 100 μm layer height and 100% infill printer settings. The straight paths from the 400 μm diameter nozzle head (printed at an angle of 45° in the horizontal x-y plane) for the top layer can be seen in FIGURE 2(a), with a close-in view shown in FIGURE 2(b). It can be seen that the resulting width of each path is approximately 460 μm, with adjacent air gaps of approximately 50 μm between paths – resulting in an average practical infill of 90% (i.e., not the 100% expected by the initial print setting).

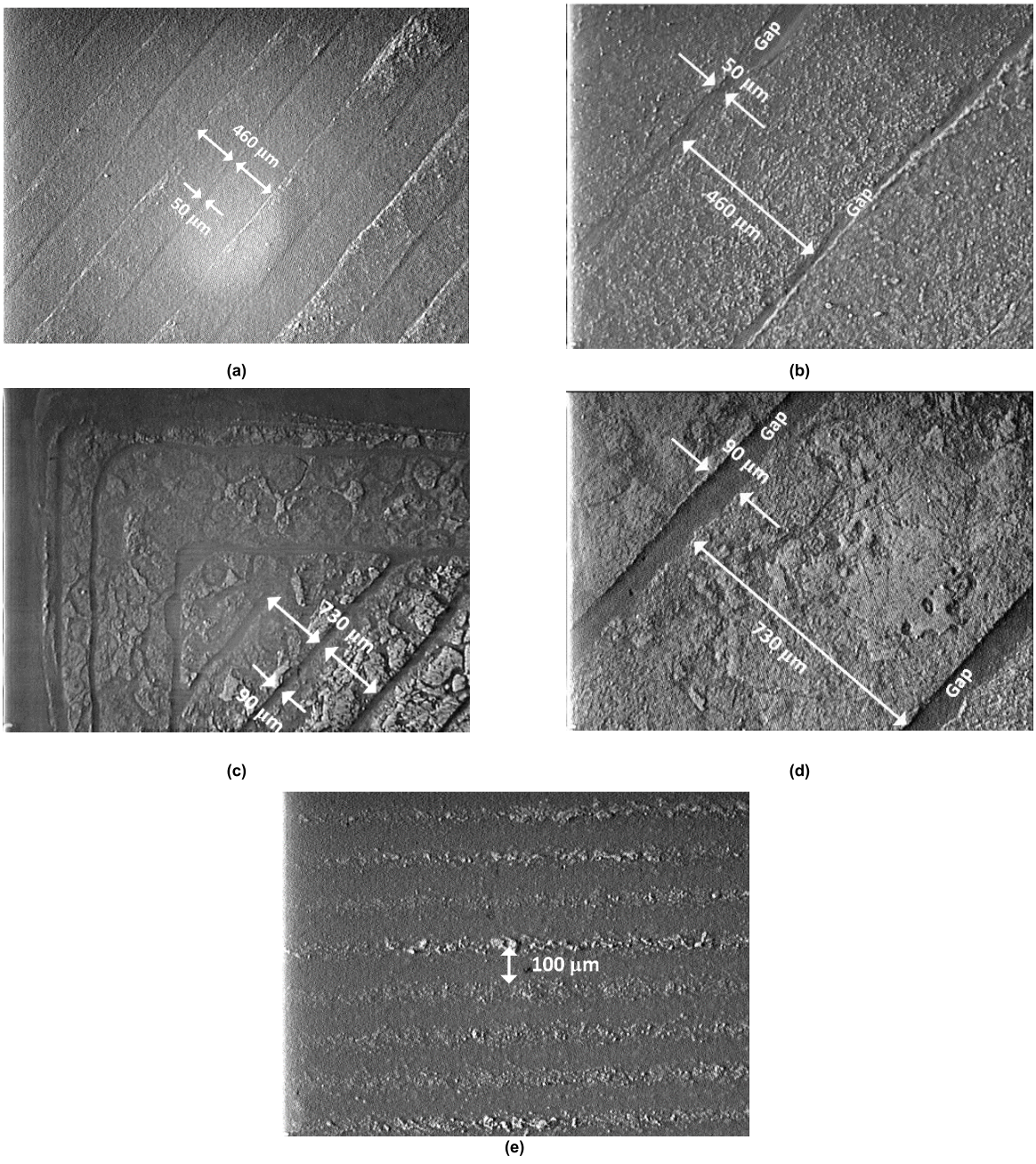

FIGURE 2. Photomicrographs of an FDM 3-D printed ABS sample under test with nominal 100 µm layer height and 100% infill printer settings: (a) top layer *x-y* plane view; (b) top layer *x-y* plane close-in view; (c) bottom layer *x-y* plane view of a corner; (d) bottom layer *x-y* plane close-in view; and (e) vertical build *x-z* plane view.

A close-in view of the bottom layer is shown in FIGURE 2(d). Here, the resulting width of each path is approximately 730 µm, with adjacent air gaps of approximately 90 µm – resulting in an average practical infill of 89%. The reason for the discrepancy between the bottom layer and subsequent layers are: (i) the recommended temperature for the glass build plate is normally between 90°C and 110°C for ABS [6]; (ii) the print nozzle temperature for the bottom layer can be set (within the software) at a higher temperature than those for subsequent layers; (iii) the print speed for the bottom layer is normally slower than for subsequent layers; and (iv) the distance between the nozzle head and the build plate is shorter for the bottom layer, when compared to subsequent layers. These settings will ensure that the building material is sufficiently molten, giving a relatively large contact area to the build plate (having wider paths), improving adhesion. In practice, with FDM 3-D printing having a 100% infill setting, voids are still created, and these are impossible to accurately control or spatially characterize.

FIGURE 2(e) shows the structure of a test sample along the vertical build z-axis. The resulting scalloping has a spatial period of 100 μm, corresponding exactly to the layer height printer setting. In practice, the sub-100% infill and the straight paths of the alternating layers printed orthogonal to one another could be described as a 3-D woodpile metamaterial (being non-homogeneous and porous). Moreover, anisotropy in the dielectric constant may be introduced due to the geometric orientation of the resulting air channels, since void densities in the orthogonal planes are expected to be different.

B. SAMPLE MEASUREMENTS

All measurements were performed by the U.K.'s National Physical Laboratory (NPL), using a vector network analyzer (VNA) configured with a pair of standard WR-90 waveguide test ports. This system enables accurate S-parameter measurements to be made across X-band. WR-90 waveguide primary reference standards, with traceability to the International System of units (SI), were used to establish reference planes for the measurements at the WR-90 waveguide test ports. This was achieved by implementing the thru-reflect-line (TRL) calibration technique [7], using: a thru (T) connection; a flush short-circuit reflection (R) connected to each test port in turn; and an air-filled quarter-wavelength thru line (L) section of waveguide, seen in FIGURE 1. The calibration was performed using an in-house calibration algorithm, employing a seven-term error-correction routine [8]. The complete measurement set-up (i.e., VNA, primary standards and calibration algorithm) is referred to as the NPL primary impedance microwave measurement system (PIMMS) [9], [10] and represents the UK's primary national standard system for S-parameter measurements. The intermediate frequency (IF) bandwidth was set at 100 Hz and no averaging was applied.

For our dielectric samples under test, the host MPRWG was the air-filled quarter-wavelength thru line section of WR-90, shown in FIGURE 1. With reference to the illustration shown in FIGURE 3, the WR-90 waveguide has nominal internal cross-sectional dimensions of $a = 22.860$ mm and $b = 10.160$ mm; the length of this reference thru line is $l = 9.626$ mm. This X-band waveguide is believed (by the UK manufacturer, Flann Microwave Ltd) to be made from solid CZ121 brass, having good-to-excellent corrosion resistance, without the need for an additional internal coating. CZ121 brass is an alpha/beta alloy composed of a maximum of 58% copper, 3% lead and the remainder being zinc [11]. The quoted dc bulk resistivity of CZ121 brass is $\rho_o|_{brass} = 6.2 \times 10^{-8}\Omega \cdot$ m [11] (which is significantly greater than that for copper, used as the default metal having $\rho_o|_{copper} = 1.7 \times 10^{-8}\Omega \cdot$ m [12] with parameter $Rho = \rho_o|_{brass}/\rho_o|_{copper} = 3.64706$ adopted within the NI AWR Design Environment Microwave Office® software [12]); giving a dc bulk conductivity of $\sigma_o = 1/\rho_o|_{brass} = 1.6129 \times 10^7$ S/m. It will be shown that the contribution of the MPRWG's internal wall conductivity loss to our measurements is significant when compared to the dielectric loss from our ABS samples under test.

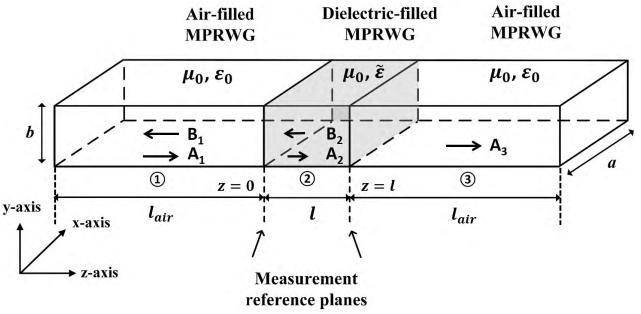

FIGURE 3. Illustration of an ideal dielectric-filled MPRWG.

Four important caveats will now be stated for the accuracy of the characterization process: (i) unless otherwise stated, the FDM 3-D printed ABS samples are considered homogeneous (no void volumes) and, thus, isotropic; (ii) it is assumed throughout that there is no uncertainly in the measurements (the impact of measurement uncertainty becomes less as the opacity of the sample increases); (iii) the empty metal-pipe rectangular waveguide loss contributions (attributed to intrinsic bulk conductivity σ and extrinsic surface tarnishing, roughness and other physical defects) are accurately represented by an effective conductivity given by $\sigma \rightarrow \sigma_o$; and (iv) the velocity of light and refractive index associated with air are the same as those in vacuum, while both also being referred to in this paper as free space.

III. FABRY-PÉROT RESONANCE MODELING

Inserting a section of dielectric into a nominally air-filled transmission line or waveguide structure, having abrupt air-dielectric boundaries, creates a Fabry-Pérot resonator; the electromagnetic discontinuities essentially behave like two imperfect mirrors. With our measurement scenario, the nominally air-filled quarter-wavelength thru line section of MPRWG filled with the sample under test exhibits a Fabry-Pérot resonance within X-band if the dielectric constant is between 2 and 3. This represents our target frequency for modeling; the spectral position of the associated characteristic '*return loss zero*' is very sensitive to the dielectric constant and not so to the loss tangent, while the associated value of return loss at this minimum is very sensitive to loss tangent and not so to dielectric constant.

It will be seen that the measured values of return loss at the Fabry-Pérot resonance frequency are slightly lower for Sample #1 and slightly higher for Sample #2 than those predicted using the various Fabry-Pérot resonance modeling approaches. This may be attributed to deviations from the first three caveats stated in Section II, as a result of having low opacity dielectric samples under test. Fortunately, it is found that the resulting errors are not significant. Here, from the principle of conservation of energy, simulated and measured absorptance of the dielectric-filled MPRWG agree when fitted to the more dominant insertion loss (unlike our original approach of using the return loss).

In this section, extraction of complex dielectric properties is performed with fitting (by visual inspection) of both dielectric constant and loss tangent values for the sample under test, such that the simulated and measured insertion losses agree at the lowest-order Fabry-Pérot resonance frequency located at the corresponding return loss zero. As a result, no phase measurements are considered with our Fabry-Pérot resonance modeling approach. It is found with low loss samples that the frequency of the return loss zero dictates the dielectric constant, while the associated value of insertion loss dictates the loss tangent.

Because of the inherent non-polar molecular nature of ABS, no dipolar (orientation) polarization relaxation frequencies should exist, which would otherwise appear spectroscopically at microwave frequencies [1]. Moreover, our FDM 3-D printed samples are essentially homogeneous. As a result of these micro and macro sample properties, the spectral response for dielectric constant should be perfectly flat across X-band (i.e., no frequency dispersion).

A. ANALYTICAL (VARIATIONAL) MODELING: M1

In any medium (unbound, transmission line or waveguide), the generic complex propagation constant is given by $\gamma = \alpha + j\beta$, where α is the attenuation constant and β is the phase constant. These constants can be accurately calculated for a dielectric-filled MPRWG using the *variational* method described in detail by Collin [13] for all transverse electric TE_{mn} modes; given here for just the TE_{m0} modes [14],

$$\gamma_{m0}^2 = \gamma_g^2 + \frac{2}{\gamma_s b}\left[\gamma_{ud}^2 + \left(\frac{2b}{a}\right)\gamma_{cm0}^2\right] \tag{1}$$

With the internal waveguide walls made from a perfect electrical conductor (PEC), i.e. with $\sigma \to \infty$, the waveguide propagation constant γ_g is related to the unbound dielectric γ_{ud} and cut-off γ_{cm0} propagation constants as,

$$\gamma_g^2 = \gamma_{ud}^2 - \gamma_{cm0}^2 \tag{2}$$

$$\gamma_{ud} = jk_{ud} \equiv j\beta_o\tilde{n} \quad \text{and} \quad \gamma_{cm0} = jk_{cm0} \equiv j\beta_{cm0} \tag{3}$$

All variables have their usual meanings: k_{ud} is the complex wavenumber within an unbound dielectric; $\beta_o = \omega/c$ is the phase constant of free space; $\omega = 2\pi f$ is the angular frequency of excitation and f is the associated excitation frequency; $c = 1/\sqrt{\mu_o\varepsilon_o}$ is the speed of light in free space, μ_o and ε_o are the permeability and permittivity of free space, respectively; the complex refractive index $\tilde{n} = \sqrt{\tilde{\mu}_r\tilde{\varepsilon}_{reff}}$ and loss tangent $tan\delta = Im\{\tilde{n}^2\}/Re\{\tilde{n}^2\}$; $\tilde{\mu}_r = \mu_r' - j\mu_r''$ is the complex relative permeability for the dielectric (it is assumed *a priori* that our ABS samples are non-magnetic and, thus, $\tilde{\mu}_r = 1$); $\tilde{\varepsilon}_{reff} = \varepsilon_{reff}' - j\varepsilon_{reff}''$ is the effective complex relative permittivity, ε_{reff}' and $tan\delta_e = tan\delta|_{\mu_r''=0} = \varepsilon_{reff}''/\varepsilon_{reff}'$ are the dielectric constant and electric loss tangent, respectively; $k_{cm0} = m\pi/a$ is the waveguide cut-off wavenumber for TE_{m0} modes; $\beta_{cm0} = \omega_{cm0}/c$ is the bound phase constant associated with the angular cut-off frequency for the air-filled waveguide, $\omega_{cm0} = 2\pi f_{cm0}$ and $f_{cm0} = k_{cm0}c/2\pi \Rightarrow f_c\sqrt{\mu_r'\varepsilon_{reff}'}$ is the cut-off frequency for the air-filled waveguide ($f_{cm0} \cong 6.55714$ GHz for the TE_{10} mode with WR-90 waveguides), with f_c being that for the dielectric-filled waveguide; γ_s is the complex propagation constant for the transverse electromagnetic (TEM) wave within the MPRWG's internal conducting metal walls (assumed here to be non-magnetic and so its permeability $\mu = \mu_o$) and Z_s is the associated surface impedance having an intrinsic bulk conductivity σ (with $\sigma \cong \sigma_o$ at X-band),

$$\gamma_s = \frac{j\omega\mu}{Z_s} \tag{4}$$

$$Z_s = \sqrt{\frac{j\omega\mu}{\sigma + j\omega\varepsilon_o}} \cong \sqrt{\frac{\omega\mu_o}{2\sigma_o}}\,(1+j) \text{ at X-band} \tag{5}$$

The wave impedance and propagation constant for the TE_{m0} modes, Z_{TEm0} and γ_{m0}, respectively, can be determined from,

$$Z_{TEm0} = \frac{j\omega\mu_o\tilde{\mu}_r}{\gamma_{m0}} \quad \text{with} \quad Z_{TEm0}^{air} = \frac{j\omega\mu_o}{\gamma_{m0}^{air}} \tag{6}$$

where, Z_{TEm0}^{air} and γ_{m0}^{air} represent the wave impedance and propagation constant for an air-filled waveguide (associated with the test ports). For the TE_{10} mode, the equivalent *power-voltage* definition for characteristic impedance Z_o gives,

$$Z_o = \left(\frac{2b}{a}\right)Z_{TE10} \quad \text{with} \quad Z_o^{air} = \left(\frac{2b}{a}\right)Z_{TE10}^{air}$$

and

$$\xi = \frac{Z_o}{Z_o^{air}} = \frac{Z_{TE10}}{Z_{TE10}^{air}} = \frac{\gamma_{10}^{air}}{\gamma_{10}}\tilde{\mu}_r \tag{7}$$

where, ξ is the normalized impedance for the medium.

The S-parameters (e.g., overall input voltage-wave reflection coefficient S_{11} and overall forward voltage-wave transmission coefficient S_{21}) for a two-port symmetrical and reciprocal network [1], in any medium are,

$$S_{11} = \frac{S_{21}}{2}\left[\xi - \frac{1}{\xi}\right]\sinh(\gamma l) \equiv S_{22} \tag{8}$$

$$S_{21} = \left\{\cosh(\gamma l) + \frac{1}{2}\left[\xi + \frac{1}{\xi}\right]\sinh(\gamma l)\right\}^{-1} \equiv S_{12} \tag{9}$$

where, l is both the length of our host MPRWG thru line and the thickness of the dielectric sample under test.

By definition, at the Fabry-Pérot resonance frequency, $\omega_{fp} = 2\pi f_{fp}$, the phase constant is,

$$\beta(\omega_{fp}) = \pi/l \tag{10}$$

$$e^{\pm j\beta(\omega_{fp})l} = -1 \tag{11}$$

$$e^{\pm\gamma(\omega_{fp})l} = -e^{\pm\alpha(\omega_{fp})l} \tag{12}$$

Therefore, at the Fabry-Pérot resonance frequency only, it can be shown that the S-parameters can be calculated from,

$$S_{11}(\omega_{fp}) = -\frac{S_{21}(\omega_{fp})}{2}\left[\xi(\omega_{fp}) - \frac{1}{\xi(\omega_{fp})}\right]\sinh\left(\alpha(\omega_{fp})\,l\right)$$

$$\approx \frac{\left[\xi(\omega_{fp})^2 - 1\right]}{\left[\xi(\omega_{fp})^2 + 1\right] + 2\xi(\omega_{fp})/\alpha(\omega_{fp})\, l}$$

$$\text{with} \quad \alpha(\omega_{fp})\, l \ll 1 \tag{13}$$

$$S_{21}(\omega_{fp}) = -\left\{\cosh(\alpha(\omega_{fp})\, l) + \frac{1}{2}\left[\xi(\omega_{fp}) + \frac{1}{\xi(\omega_{fp})}\right]\sinh(\alpha(\omega_{fp})\, l)\right\}^{-1}$$

$$\approx -\left\{1 + \frac{\alpha(\omega_{fp})\, l}{2}\left[\xi(\omega_{fp}) + \frac{1}{\xi(\omega_{fp})}\right]\right\}^{-1}$$

$$\text{with} \quad \alpha(\omega_{fp})\, l \ll 1 \tag{14}$$

With this distributed-element model, the theoretical phase angle $\angle S_{21}(\omega_{fp}) = -\pi$ and the corresponding differential-phase group delay can be calculated using (9) from,

$$\tau_g(\omega_{fp}) = -\frac{\partial \angle S_{21}(\omega)}{\partial \omega}\bigg|_{\omega=\omega_{fp}} \tag{15}$$

Therefore, at the Fabry-Pérot resonance frequency with low-loss samples, $\alpha(\omega_{fp})\, l \cong 0$ and $e^{\pm\alpha(\omega_{fp})l} \cong 1$, and (13) and (14) respectively giving a return loss zero with $S_{11}(\omega_{fp}) \cong 0$ and $S_{21}(\omega_{fp}) \cong -1$ with $\angle S_{21}(\omega_{fp}) \cong -\pi$.

B. ANALYTICAL (TEXTBOOK) MODELING: M2

Simplified engineering textbook approximations [15], [16] that generally assume operation above the waveguide mode's lower cut-off frequency and under lossless dielectric and metal conditions (with identities explicitly indicated by $\Rightarrow$) serve as a useful sanity check, especially here where low loss dielectrics are being characterized in-band with low loss air-filled MPRWG. It will be found that Microwave Office® [12] uses such expressions [15], which proves useful for accurately validating subsequent calculations.

Propagation constant γ, wavenumber k and wavelength $\tilde{\lambda}$ are all generic complex variables related to one another by,

$$\gamma = jk = j\frac{2\pi}{\tilde{\lambda}} \tag{16}$$

With a dielectric-filled MPRWG, (1) can be greatly simplified with PEC internal waveguide walls. Thus, using simple trigonometry, the propagation constant for the unbound dielectric γ_{ud} can be expressed in terms of the longitudinal waveguide propagation constant γ_g and transverse waveguide cut-off propagation constant γ_{cm0} as,

$$\gamma_{ud}^2 = \gamma_g^2 + \gamma_{cm0}^2 \tag{17}$$

giving the following wavenumber and wavelength relationships from (2) with (16),

$$k_g^2 = k_{ud}^2 - k_{cm0}^2 \tag{18}$$

and,

$$\frac{1}{\tilde{\lambda}_g^2} = \frac{1}{\tilde{\lambda}_{ud}^2} - \frac{1}{\lambda_{cm0}^2} \tag{19}$$

where,

$$\tilde{\lambda}_{ud} = \frac{\lambda_o}{\tilde{n}} \quad \text{and} \quad \lambda_o = \frac{c}{f} = \frac{2\pi}{\beta_0} \tag{20}$$

$$\lambda_{cm0} = \frac{c}{f_{cm0}} = \frac{2\pi}{k_{cm0}} \to \frac{2a}{m} \qquad \text{TE}_{\text{m0}} \text{ modes} \tag{21}$$

The complex guided-wavelength is,

$$\tilde{\lambda}_g = \frac{\tilde{\lambda}_{ud}}{\sqrt{1 - \left(\frac{\tilde{\lambda}_{ud}}{\lambda_{cm0}}\right)^2}} = \frac{\lambda_o}{\sqrt{\tilde{n}^2 - \left(\frac{\lambda_o}{\lambda_{cm0}}\right)^2}} \tag{22}$$

The physical guided-wavelength λ_g is related to complex guided-wavelength $\tilde{\lambda}_g$ by,

$$\frac{1}{\lambda_g} = Re\left\{\frac{1}{\tilde{\lambda}_g}\right\} \tag{23}$$

However, by adopting the lossless dielectric approximation, with $\tilde{n}^2 = \tilde{\mu}_r \tilde{\varepsilon}_{reff} \Rightarrow \mu_r' \varepsilon_{reff}'$, the textbook approximation for guided-wavelength is,

$$\tilde{\lambda}_g \Rightarrow \lambda_g = \frac{\lambda_o}{\sqrt{\mu_r' \varepsilon_{reff}' - \left(\frac{f_{cm0}}{f}\right)^2}} = \frac{\lambda_o/\sqrt{\mu_r' \varepsilon_{reff}'}}{\sqrt{1 - \left(\frac{f_c}{f}\right)^2}} \tag{24}$$

The complex phase constant $\tilde{\beta} \equiv k_g = 2\pi/\tilde{\lambda}_g$ is given by,

$$\tilde{\beta} = k_{ud}\sqrt{1 - \left(\frac{\tilde{\lambda}_{ud}}{\lambda_{cm0}}\right)^2} = \beta_0\sqrt{\tilde{n}^2 - \left(\frac{\lambda_o}{\lambda_{cm0}}\right)^2} \tag{25}$$

Giving the textbook approximation for phase constant,

$$\tilde{\beta} \Rightarrow \beta = \beta_0\sqrt{\mu_r' \varepsilon_{reff}' - \left(\frac{f_{cm0}}{f}\right)^2} = \beta_0\sqrt{\mu_r' \varepsilon_{reff}'}\sqrt{1 - \left(\frac{f_c}{f}\right)^2} \tag{26}$$

For a lossless waveguide, the lowest-order Fabry-Pérot resonance frequency can be calculated by setting guided-wavelength $\lambda_g(f_{fp}) = 2\pi/\beta(f_{fp}) = 2l$. As a result, it can be shown for TE_{m0} modes that,

$$f_{fp} \Rightarrow \frac{c/\sqrt{\mu_r' \varepsilon_{reff}'}}{2l}\sqrt{1 + (ml/a)^2} \tag{27}$$

For TE_{m0} modes, the complex wave impedance Z_{TEm0} for a dielectric-filled MPRWG is given by,

$$Z_{TEm0} = \frac{j\omega\mu_o\tilde{\mu}_r}{\gamma_{m0}} = \frac{\eta}{\sqrt{1 - \left(\frac{\tilde{\lambda}_{ud}}{\lambda_{cm0}}\right)^2}} = \frac{\eta_o\tilde{\mu}_r}{\sqrt{\tilde{n}^2 - \left(\frac{\lambda_o}{\lambda_{cm0}}\right)^2}} \tag{28}$$

where, the intrinsic impedance of the unbound dielectric medium $\eta = \sqrt{\mu_0\tilde{\mu}_r/\varepsilon_0\tilde{\varepsilon}_{reff}} \Rightarrow \eta_0\sqrt{\mu_r'/\varepsilon_{reff}'}$ and $\eta_0 = \sqrt{\mu_0/\varepsilon_0}$ is the intrinsic impedance of free space.

The textbook approximation for TE_{m0} mode wave impedance is now,

$$Z_{TEm0} \Rightarrow \frac{\eta_o \mu'_r}{\sqrt{\mu'_r \varepsilon'_{reff} - \left(\frac{f_{cm0}}{f}\right)^2}} = \frac{\eta_o \sqrt{\mu'_r / \varepsilon'_{reff}}}{\sqrt{1 - \left(\frac{f_c}{f}\right)^2}} \tag{29}$$

With air-filled MPRWGs, the associated wave impedance is,

$$Z^{air}_{TEm0} = \frac{\eta_0}{\sqrt{1 - \left(\frac{f_{cm0}}{f}\right)^2}} \tag{30}$$

For completeness, with transverse magnetic TM_{m0} modes, the complex wave impedance Z_{TMm0} for a dielectric-filled MPRWG is given by,

$$Z_{TMm0} = \frac{\gamma_{m0}}{j\omega\varepsilon_0 \tilde{\varepsilon}_{reff}} = \frac{\eta_o}{\tilde{\varepsilon}_{reff}} \sqrt{\tilde{n}^2 - \left(\frac{\lambda_o}{\lambda_{cm0}}\right)^2} \tag{31}$$

The textbook approximation for TM_{m0} mode wave impedance is,

$$\begin{aligned} Z_{TMm0} &\Rightarrow \frac{\eta_o}{\varepsilon'_{reff}} \sqrt{\mu'_r \varepsilon'_{reff} - \left(\frac{f_{cm0}}{f}\right)^2} \\ &= \eta_o \sqrt{\left(\frac{\mu'_r}{\varepsilon'_{reff}}\right)\left[1 - \left(\frac{f_c}{f}\right)^2\right]} \end{aligned} \tag{32}$$

With air-filled MPRWGs, the associated wave impedance is,

$$Z^{air}_{TMm0} = \eta_0 \sqrt{1 - \left(\frac{f_{cm0}}{f}\right)^2} \tag{33}$$

The normalized impedances for various media can now be approximated to,

$$\xi = \begin{cases} \dfrac{\eta}{\eta_0} \Rightarrow \sqrt{\dfrac{\mu'_r}{\varepsilon'_{reff}}} & \text{free} - \text{space TEM waves} \\ & \text{with (quasi}-\text{) optics} \\ \dfrac{Z_{TEm0}}{Z^{air}_{TEm0}} \Rightarrow \sqrt{\dfrac{\mu'_r}{\varepsilon'_{reff}}} \sqrt{\dfrac{f^2 - f^2_{cm0}}{f^2 - f^2_c}} & \text{TE modes in} \\ & \text{lossless waveguides} \\ \dfrac{Z_{TMm0}}{Z^{air}_{TMm0}} \Rightarrow \sqrt{\dfrac{\mu'_r}{\varepsilon'_{reff}}} \sqrt{\dfrac{f^2 - f^2_c}{f^2 - f^2_{cm0}}} & \text{TM modes in} \\ & \text{lossless waveguides} \end{cases} \tag{34}$$

From (27), it will be found that for the TE_{m0} mode at the lowest-order Fabry-Pérot resonance frequency,

$$\left(\frac{f_{cm0}}{f_{fp}}\right)^2 \Rightarrow \frac{\mu'_r \varepsilon'_{reff}}{m^2 + (a/l)^2} \tag{35}$$

giving, for the TE_{10} mode,

$$\beta(f_{fp}) \cong \beta_0(f_{fp}) \sqrt{\frac{\mu'_r \varepsilon'_{reff}}{1 + (l/a)^2}} \tag{36}$$

$$\lambda_g(f_{fp}) \cong \lambda_0(f_{fp}) \sqrt{\frac{1 + (l/a)^2}{\mu'_r \varepsilon'_{reff}}} \tag{37}$$

$$Z_{TE10}(f_{fp}) \cong \eta_0 \sqrt{\left(\frac{\mu'_r}{\varepsilon'_{reff}}\right)\left[1 + (l/a)^2\right]} \tag{38}$$

$$Z^{air}_{TE10}(f_{fp}) \cong \frac{\eta_0 \sqrt{1 + (l/a)^2}}{\sqrt{1 + \left(1 - \mu'_r \varepsilon'_{reff}\right)(l/a)^2}} \tag{39}$$

$$\begin{aligned} \xi_{TE10}(f_{fp}) &= \frac{Z_{TE10}(f_{fp})}{Z^{air}_{TE10}(f_{fp})} \\ &\cong \sqrt{\left(\frac{\mu'_r}{\varepsilon'_{reff}}\right)\left[1 + \left(1 - \mu'_r \varepsilon'_{reff}\right)\left(\frac{l}{a}\right)^2\right]} \end{aligned} \tag{40}$$

For a medium that is terminated at both ends by the same reference port impedance Z_T, quality (Q-)factor can be broken down into constituent components; loaded Q_L and unloaded Q_U Q-factors are related by,

$$\frac{1}{Q_L} = \frac{1}{Q_U} + \frac{1}{Q_e}$$

where

$$\frac{1}{Q_U} = \frac{1}{Q_c} + \frac{1}{Q_d} + \frac{1}{Q_r} \tag{41}$$

where, Q_e, Q_c, Q_d and Q_r are the respective Q-factors associated with the external (e) loading from the terminating impedances and contributions due to conductive (c), dielectric (d) and radiative (r) losses. With a MPRWG, there is no leakage of radiation and, thus, $Q_r \to \infty$ and so this term can be ignored. It can be shown that for an arbitrary length of uniform medium,

$$Q_U = \frac{\beta}{2\alpha} = \frac{\pi}{\alpha \lambda_g} \to Q_U(f_{fp}) = \frac{\pi}{2\alpha(f_{fp})\, l} \tag{42}$$

The *power-loss* approximation for attenuation constant α of a dielectric-filled transmission line or waveguide has,

$$\alpha \cong \alpha_c + \alpha_d \tag{43}$$

where, α_c and α_d are the independent contributions to the attenuation constant from the conductor and dielectric, respectively. Therefore,

$$Q_c(f_{fp}) \cong \frac{\pi}{2\alpha_c(f_{fp})\, l} \quad \text{and} \quad Q_d(f_{fp}) \cong \frac{\pi}{2\alpha_d(f_{fp})\, l} \tag{44}$$

The following textbook expressions will now assume perfect impedance matching at the measurement reference planes (with identities explicitly indicated by $\rightsquigarrow$), such that the Z^{air}_{TE10} and Z^{air}_0 terminating impedances are replaced by Z_{TE10} and Z_0, respectively, and, thus, $\xi \rightsquigarrow 1$.

If the dielectric insert is now assumed to be lossless then the attenuation constant, which only considers the conduction loss contribution from the internal metal waveguide walls, is obtained from the following textbook reflection-less approximation for the TE_{10} mode,

$$\alpha_c \rightsquigarrow \frac{Rs(f)\, Z_{TE10}}{\eta^2 b} \cdot \left[1 + \left(\frac{2b}{a}\right)\left(\frac{f_c}{f}\right)^2\right] \quad \text{with} \quad tan\delta = 0 \tag{45}$$

where, the classical skin-effect surface resistance approximation (which ignores both the displacement current term and conductivity having relaxation-effect dispersion) for non-magnetic metals is given by,

$$R_s(f) \cong \sqrt{\pi f \mu_0 \rho_o} \quad \text{at X-band} \tag{46}$$

Calculating α_c using (45) is only valid when there are no reflection losses (i.e., both ports are terminated by $Z_T = Z_0$); otherwise, in our case, there will be ∼16% increase in value when terminated by the calibrated VNA with $Z_T = Z_0^{air}$.

The opacity [1] of the dielectric sample under test is $2\alpha_d l \rightarrow \alpha_d(f_{fp})\,\lambda_g(f_{fp})$ [Np/λ_g] at the lowest-order Fabry-Pérot resonance frequency, where $2\alpha_d l \ll 1$ with our samples under test. Here, the attenuation constant can be greatly simplified using a textbook reflection-less approximation that only considers the loss contribution from the dielectric insert. With a PEC-walled MPRWG and dielectric insert having $\mu_r'' = 0$,

$$\alpha_d \rightsquigarrow \frac{\sigma_d}{2} Z_{TE} \quad \text{with PEC walls} \tag{47}$$

where, $\sigma_d = \omega\varepsilon_0\varepsilon_{reff}'' = \omega\varepsilon_0\varepsilon_{reff}'/Q_{0e}$ is the effective conductivity and $Q_{0e} = 1/tan\delta_e$ is the intrinsic Q-factor for an unbound non-magnetic dielectric. Using (38), for the TE_{10} mode, it can be shown that,

$$\alpha_d(f_{fp}) \cong \frac{\beta_0(f_{fp})}{2Q_{0e}} \sqrt{\left(\frac{\mu_r'}{\varepsilon_{reff}'}\right)\left[1 + (l/a)^2\right]} \tag{48}$$

and,

$$Q_d(f_{fp}) = \frac{\beta(f_{fp})}{2\alpha_d(f_{fp})} = \frac{\pi}{\alpha_d(f_{fp})\,\lambda_g(f_{fp})} = \frac{Q_{0e}}{1 + (l/a)^2} \tag{49}$$

Finally, the insertion loss IL of the dielectric-filled waveguide is given by,

$$IL\,[\text{dB}] = -10log_{10}\left\{|S_{21}|^2\right\} \tag{50}$$

As a result, it will be respectively seen from (9) and (14) that,

$$S_{21} \rightsquigarrow e^{-\gamma l} \quad \text{and} \quad S_{21}(f_{fp}) \rightsquigarrow -e^{-\alpha(f_{fp})l} \tag{51}$$

giving,

$$\alpha(f_{fp}) \rightsquigarrow \frac{IL(f_{fp})\,[\text{dB}]}{20log_{10}\{e\}\,l} \quad \text{and } Q_U(f_{fp}) \rightsquigarrow \frac{13.644}{IL(f_{fp})\,[\text{dB}]} \tag{52}$$

The results from Fabry-Pérot resonance modeling strategies M1 and M2 are summarized in TABLE 1. As expected, the Fabry-Pérot resonance frequencies and associated insertion losses can be easily emulated, with very little discrepancy between the results from the accurate *variational* and simplified *textbook* approaches; the only exception being the unloaded Q-factor, which is approximately 3% too high with the former and 13% too low with the latter approaches.

With our experimental setup, with M2, it is found that the conduction loss contribution to the total attenuation constant is approximately 6-8%. Moreover, without a dielectric insert, the air-filled MPRWG will have a calculated attenuation constant of $\alpha_c \cong 0.0223$ Np/m at 11.1 GHz, corresponding to a reflection-less specific attenuation of 0.19 dB/m; this is commensurate with a 5 inch long waveguide having a previously measured specific attenuation of 0.16 dB/m.

TABLE 1. Fabry-Pérot resonance simulation results with analytical modeling M1 and M2.

Parameter at ω_{fp}		Sample #1	Sample #2
Measurements	f_{fp} [GHz]	11.080	11.130
	$\|S_{11}\|$ [dB]	-59.8031	-47.1815
	$\|S_{21}\|$ [dB]	-0.03812	-0.02997
	τ_g [ps]	59.2042	59.9557
	Q_L	2.061	2.096
	Q_U	470.6	608.6
	Q_e	2.070	2.104
M1: *Variational* Modeling (Using measured f_{fp}, $\|S_{21}\|$)	ε_{reff}'	2.3250	2.3045
	$tan\delta_e \times 10^4$	19.250	14.720
	f_{fp} [GHz]	11.080	11.130
	$\|S_{11}\|$ [dB]	-53.0878	-55.3576
	$\|S_{21}\|$ [dB]	-0.03827	-0.02974
	τ_g [ps]	61.4761	61.0096
	Q_L	2.140	2.124
	Q_U	486.7	621.2
	Q_e	2.149	2.131
M2: Textbook Modeling (Using f_{fp}, ε_{reff}' and $tan\delta_e$ from M1)	Z_{TE10}^{air} [Ω]	467.358	466.233
	Z_0^{air} [Ω]	415.429	414.429
	Z_{TE10} [Ω]	268.085	269.271
	Z_0 [Ω]	238.297	239.352
	ξ	0.57362	0.57755
	σ_d [mS/m]	2.7588	2.1004
	α_d [Np/m]	0.3698	0.2828
	Q_d	441.3	577.0
	R_s [mΩ/□]	52.077	52.194
	α_c [Np/m]	0.0255	0.0255
	Q_c	6393.1	6407.3
	αl [mNp]	3.8052	2.9677
	Q_U	412.8	529.3
	$\|S_{11}\|$ [dB]	-53.0898	-55.3586
	$\|S_{21}\|$ [dB]	-0.03827	-0.02975
	Q_L	1.815	1.810
	Q_e	1.823	1.816

When compared to measurements (having a frequency resolution of 0.01 GHz), the simulated return loss is increased by ∼7 dB for Sample #1 and decreased by ∼8 dB for Sample #2. The measured differential-phase group delay is 3.7% and 1.7% less than predicted for Sample #1 and Sample #2, respectively; with a commensurate reduction in measured loaded and unloaded Q-factors. This could be attributed to non-homogeneous samples (with significant void volumes); being reduced in effective length by 356 μm and 164 μm for Sample #1 and Sample #2, respectively.

In summary, with analytical Fabry-Pérot resonance modeling M1, the extracted sample average fitted dielectric constant and loss tangent for our ABS are approximately 2.31 and 17×10^{-4}, respectively, at 11.1 GHz.

C. EQUIVALENT-CIRCUIT (MPRWG) MODELING: M3

With our X-band tunable phase shifter [3], the dielectric flap insert was designed using fixed values for dielectric

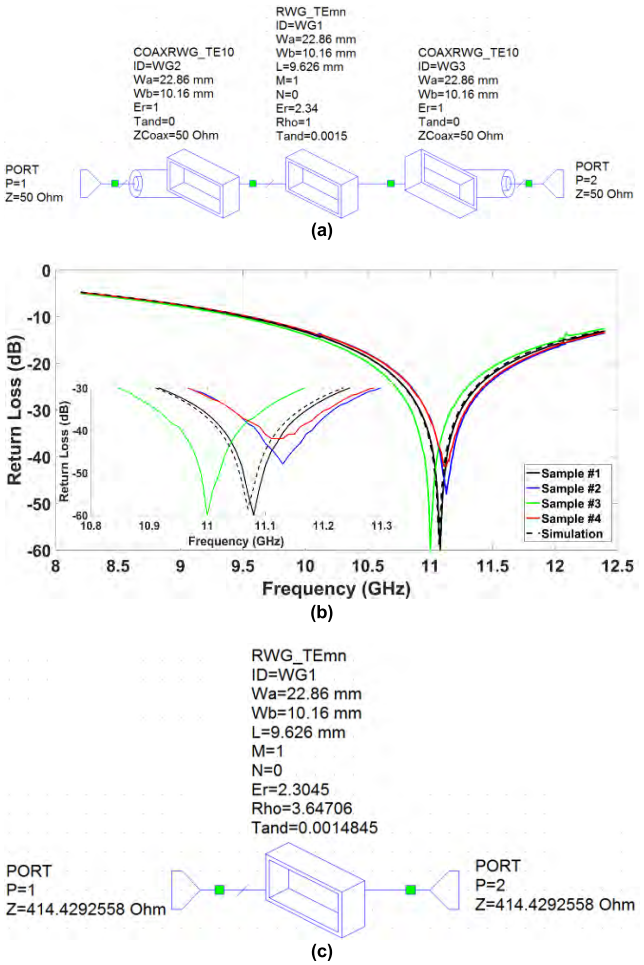

FIGURE 4. Circuit-based *Fabry-Pérot resonance brute-force* modeling approach with both ports effectively terminated by $Z_T = Z_0^{air}$ in Microwave Office®: (a) original MPRWG equivalent circuit model [3]; (b) measurements from four individual dielectric samples and original simulated response [3]; and (c) new simplified MPRWG equivalent circuit model for Sample #2 at its Fabry-Pérot resonance frequency of 11.13 GHz.

constant and loss tangent (2.34 and 15×10^{-4}, respectively); extracted using a simple copper-walled MPRWG equivalent circuit model within Microwave Office®, shown in FIGURE 4(a).

This distributed-element model consists of a MPRWG element, having an equivalent characteristic impedance Z_0 with *power-voltage* definition (7) using analytical (textbook) modeling with (29), and ideal MPRWG-to-coaxial transitions; all set for the TE_{10} mode [15]. The modeled input return loss frequency responses were compared to those measured with this *brute-force* modeling approach; with [3], fitting only to the return loss and ignoring insertion loss.

It can be clearly seen that while every effort was made to create identical samples, the input return loss frequency responses are noticably different. From the small cluster of results seen in FIGURE 4(b), a model was loosely fitted to the Fabry-Pérot resonance frequency return loss minima of Sample #1, as it was reasonable to choose a mid-sample response between Samples #2 and #3; with Sample #4 considered too much of an outlier to be considered further. Therefore, the original sample average extracted values for dielectric constant and loss tangent of 2.34 and 15×10^{-4}, respectively, were less than those of 2.54 and 151×10^{-4} previously published in the open literature for pure ABS at 10 GHz [17]. The expected loss tangent from [17] was considered too lossy to be a useful dielectric for most applications; however, this is an order of magnitude greater than our initial extracted value.

With low loss samples, measurement accuracy can be compromised by the inherent systematic and random errors that are generally associated with a calibrated instrument [1]. In practice, VNA measurement quality can be improved by repeating the calibration and sample measurement cycle. One indicator for high quality measurements is to check the equality of the forward and reverse voltage-wave transmission coefficients for reciprocal samples under test, at all frequencies. While this may appear obvious, it can be difficult to maintain $S_{21}(\omega) = S_{12}(\omega)$ under very low loss conditions. For this reason, only the measurements for Samples #1 and #2 were considered of sufficient quality to warrant further investigation.

By default, within Microwave Office®, since the equivalent *power-voltage* definition for characteristic impedance is adopted, $Z_0^{air}(\omega_{fp})$ must be used as the system's reference impedance for both ports, as explicitly shown in FIGURE 4(c).

D. EQUIVALENT-CIRCUIT (RLC) MODELING: M4

A single resonator's loaded and unloaded Q-factors, in this case associated with the Fabry-Pérot resonances, $Q_L(\omega_{fp})$ and $Q_U(\omega_{fp})$, respectively, can be calculated from the measured voltage-wave transmission coefficient $S_{21}(\omega_{fp})$,

$$Q_L(\omega_{fp}) = \frac{\omega_{fp}}{2}\tau_g(\omega_{fp}) \tag{53}$$

$$Q_U(\omega_{fp}) = \frac{Q_L(\omega_{fp})}{1-|S_{21}(\omega_{fp})|} \tag{54}$$

and, therefore, using (41) it can be easily shown that,

$$Q_e(\omega_{fp}) = \frac{Q_U(\omega_{fp})\,Q_L(\omega_{fp})}{Q_U(\omega_{fp}) - Q_L(\omega_{fp})} = \frac{Q_L(\omega_{fp})}{|S_{21}(\omega_{fp})|} \tag{55}$$

where, $\tau_g(\omega_{fp}) = 2Z(\omega_{fp})\,C$ and $Z(\omega_{fp}) = R//Z_0^{air}(\omega_{fp})/2$ for the lumped-element RLC equivalent circuit model shown in FIGURE 5.

From these Q-factors, the equivalent RLC lumped-element values can be extracted using,

$$Q_L(\omega_{fp}) = \begin{cases} \dfrac{Z(\omega_{fp})}{\omega_{fp}L} \\ \omega_{fp}CZ(\omega_{fp}) \end{cases} \tag{56}$$

$$Q_U(\omega_{fp}) = \begin{cases} \dfrac{R}{\omega_{fp}L} \\ \omega_{fp}CR \end{cases} \tag{57}$$

$$Q_e(\omega_{fp}) = Q_e(\omega_{fp})_{①}//Q_e(\omega_{fp})_{②} = \begin{cases} \dfrac{Z_0^{air}(\omega_{fp})/2}{\omega_{fp}L} \\ \omega_{fp}CZ_0^{air}(\omega_{fp})/2 \end{cases} \tag{58}$$

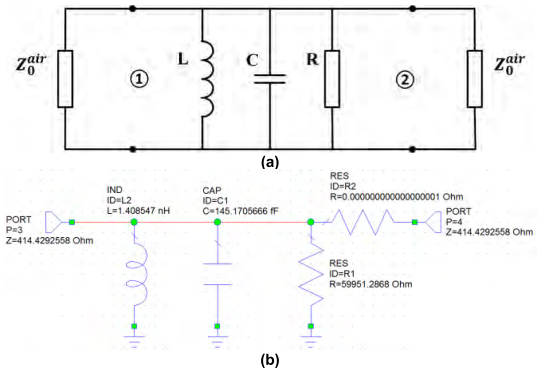

FIGURE 5. Lumped-element RLC equivalent circuit model terminated at both ports by $Z_T = Z_0^{air}(\omega_{fp})$: (a) generic; and (b) lumped-element RLC equivalent circuit model in Microwave Office® for Sample #2 at its Fabry-Pérot resonance frequency of 11.13 GHz.

where, subscripts ① and ② refer to the individual contributions from the respective input and output terminated ports. By taking the ratio of the Q-factors in (56) and (57), and substituting into (54), it can be shown that,

$$R = \frac{Z_0^{air}(\omega_{fp})}{2}\left[\frac{|S_{21}(\omega_{fp})|}{1-|S_{21}(\omega_{fp})|}\right] \tag{59}$$

$$L = \frac{Z_0^{air}(\omega_{fp})\,|S_{21}(\omega_{fp})|}{\omega_{fp}^2\tau_g(\omega_{fp})} = \frac{2Z(\omega_{fp})}{\omega_{fp}^2\tau_g(\omega_{fp})} = \frac{R}{\omega_{fp}Q_U(\omega_{fp})} \tag{60}$$

$$C = \frac{\tau_g(\omega_{fp})}{Z_0^{air}(\omega_{fp})\,|S_{21}(\omega_{fp})|} = \frac{\tau_g(\omega_{fp})}{2Z(\omega_{fp})} = \frac{Q_U(\omega_{fp})}{\omega_{fp}R} = \frac{1}{\omega_{fp}^2 L} \tag{61}$$

Note that the extracted RLC lumped-element values do not differentiate between the loss contributions from the conducting metal wall and dielectric insert (i.e., they include the combined losses associated with the dielectric-filled waveguide section). Also, the RLC values are extracted from S-parameter measurements having a specific reference port impedance $Z_T = Z_0^{air}(\omega_{fp})$. Therefore, changing Z_T (with any previously extracted RLC values) will result in new S-parameters; changing $Q_L(\omega_{fp}) = f(Z_T)$, but not changing $Q_U(\omega_{fp}) \neq f(Z_T)$.

It can then be shown that the corresponding S-parameters are given as,

$$S_{11}^{RLC}(\omega_{fp}) = -\frac{1}{1+2R/Z_0^{air}(\omega_{fp})} \tag{62}$$

$$S_{21}^{RLC}(\omega_{fp}) = 1 + S_{11}^{RLC}(\omega_{fp}) \tag{63}$$

With this lumped-element model, the theoretical phase angle $\angle S_{21}^{RLC}(\omega_{fp}) = 0$; clearly being fundamentally different to $-\pi$ predicted by the distributed-element model.

The results from Fabry-Pérot resonance modeling strategies M3 (using the model in FIGURE 4(c)) and M4 (using the model in FIGURE 5(b)) are summarized in TABLE 2. Again, as expected, the Fabry-Pérot resonance frequencies and associated insertion losses can be easily emulated, with very little discrepancy between the results from the distributed- and lumped-element approaches.

TABLE 2. Fabry-Pérot resonance simulation results with equivalent circuit modeling M3 and M4.

Parameter at ω_{fp}		Sample #1	Sample #2
M3: Distributed-element MPRWG (Using measured f_{fp}, $\lvert S_{21}\rvert$)	Z_0^{air} [Ω]	415.429	414.429
	ε'_{reff}	2.3250	2.3045
	$tan\delta_e \times 10^4$	19.170	14.845
	f_{fp} [GHz]	11.08	11.13
	$\lvert S_{11}\rvert$ [dB]	-53.09	-55.29
	$\lvert S_{21}\rvert$ [dB]	-0.03812	-0.02997
	τ_g [ps]	61.473	61.007
	Q_L	2.140	2.133
	Q_U	488.6	619.3
	Q_e	2.149	2.140
M4: Lumped-element RLC (Using measured f_{fp}, $\lvert S_{21}\rvert$ and τ_g)	Z_o^{air} [Ω]	415.429	414.429
	R [kΩ]	47.225	59.951
	L [nH]	1.4414	1.4085
	C [fF]	143.140	145.171
	f_{fp} [GHz]	11.080	11.130
	$\lvert S_{11}^{RLC}\rvert$ [dB]	-47.17	-49.26
	$\lvert S_{21}^{RLC}\rvert$ [dB]	-0.03812	-0.02997
	τ_g [ps]	59.204	59.956
	Q_L	2.061	2.096
	Q_U	470.9	608.6
	Q_e	2.070	2.104

When compared to analytical modeling, the equivalent circuit model return losses are the same for the distributed-element approach but ∼6 dB higher with the lumped-element approach; attributed to the fundamental difference between the distributed- and lumped-element natures of these equivalent circuit models. As expected, with the distributed-element approach, the differential-phase group delay and associated Q-factors are the same as those found with the *variational* method; while with the lumped-element approach they are identical to those from measurements.

In summary, with distributed-element equivalent circuit Fabry-Pérot resonance modeling M3, the independently extracted sample average fitted dielectric constant and loss tangent for our ABS are 2.31 and 17×10^{-4}, respectively, at 11.1 GHz, supporting our analytical modeling M1 results.

The normalized power reflectance $\mathcal{R}$ and transmittance $\mathcal{T}$ for a dielectric-filled MPRWG can be equated directly to the measured two-port S-parameters as follows [1], but only if the reference port impedance Z_T is purely real (e.g., η_0 for free-space TEM waves with (quasi-)optics or Z_{TEm0}^{air} using (30) for TE modes with lossless waveguides),

$$\mathcal{R} \equiv |S_{11}|^2 \tag{64}$$

$$\mathcal{T} \equiv |S_{21}|^2 \tag{65}$$

S-parameter values are constrained by the principle of conservation of energy, with $\mathcal{R}+\mathcal{A}+\mathcal{T}=1$, where absorptance $\mathcal{A}$ is,

$$\mathcal{A} \equiv 1 - |S_{11}|^2 - |S_{21}|^2 \tag{66}$$

It is interesting to note that with equivalent-circuit RLC modeling, at the Fabry-Pérot resonance frequency, by inserting (63) into (66), the corresponding absorptance is $\mathcal{A}^{RLC}(\omega_{fp}) \equiv 2\left|S_{11}^{RLC}(\omega_{fp})\right|\left|S_{21}^{RLC}(\omega_{fp})\right| \neq \mathcal{A}$, since $\left|S_{11}^{RLC}(\omega_{fp})\right| \neq \left|S_{11}(\omega_{fp})\right|$ seen in TABLES 1 and 2.

E. NUMERICAL (FINITE-ELEMENT) MODELING: M5

Finite-element based numerical solvers within *COMSOL Multiphysics*® [18] were used to perform numerical modeling of the waveguide structure, illustrated in FIGURE 3, considering both the finite conductivity of the waveguide's internal walls and dielectric sample losses. The RF Module within *COMSOL Multiphysics*® provides a steady-state frequency-domain solver (which is a rigorous full-wave simulator that solves Maxwell's equations with a solution that is the superposition of all possible modes; with a MPRWG: TE_{mn}, TE_{mnp}, TM_{mn}, TM_{mnp}) and an eigenmode solver (which is a rigorous simulator that solves Maxwell's equations for individual standing-wave modes; with a MPRWG: TE_{mnp} and TM_{mnp}). The former rigorously solves Maxwell's equations at each frequency, subject to an external steady-state sinusoidal excitation at the ports. With the latter, the magnitude of the generated complex eigenfrequency $\tilde{f}_{fp} = f'_{fp} + jf''_{fp}$ gives the driven (undamped) resonance frequency $f_{fp} = \left|\tilde{f}_{fp}\right|$ corresponding to that seen with the former in the frequency domain [19].

Both propagating-wave Fabry-Pérot mode resonances and standing-wave *'open-box'* mode resonances, associated with the dielectric-filled waveguide section, were simulated using frequency-domain and eigenmode solvers, respectively.

The frequency-domain solver computes the steady-state response of the structure at a single excitation frequency. Our simulations had a frequency resolution of 0.01 GHz with 421 frequency points equally spaced between 8.2 and 12.4 GHz. Reflection-less waveguide ports are generally located at the ends of a structure (in our case a rectangular surface boundary if defined, which is excited by a single mode). S-parameters are computed from reflected and transmitted fields at these ports, with respect to a predefined incident field excitation at one of the ports. There are two approaches that can be adopted for the numerical modeling of our experimental setup using *COMSOL Multiphysics*®; both require post-processing of the S-parameters.

The first approach is to simulate the complete structure illustrated in FIGURE 3 directly, by defining ports at the ends of the air-filled waveguide sections and then de-embedding these sections to move the S-parameter reference planes from the ports to the dielectric sample under test. In this case, the reference port impedance is the wave impedance of the TE_{10} mode within a lossless air-filled waveguide (i.e., $Z_T = Z^{air}_{TE10}$, calculated using (30)). This approach has the advantage that de-embedding is simple for air-filled waveguide sections and only requires multiplication of simulated S-parameters by $e^{+2\gamma^{air}_{10} l_{air}}$, where l_{air} is the length of both air-filled sections (with $l_{air} = l$ in our simulations). The main disadvantage is that there is a computational overhead, as the air-filled sections must also be simulated. It should be noted that while it is possible to reduce l_{air}, a smaller distance between the waveguide port and air-dielectric boundary require a denser mesh; incurring a larger overhead in computation time and memory, when compared to a longer air-filled section.

The second approach only simulates the dielectric-filled waveguide section. In this case the reference port impedance is the wave impedance of the TE_{10} mode within the dielectric-filled waveguide (i.e., $Z_T = Z_{TE10}$). The S-parameters obtained must then be renormalized to the impedance of the TE_{10} mode in lossless air-filled waveguide. This approach has the advantage that the simulated structure is just a rectangular block, thus, resulting in reduced simulation time and memory. The main disadvantage is that renormalization of S-parameters is not straight-forward and requires matrix manipulation [20].

Numerical finite-element simulations were run on a dual-core Intel Xeon E5-2665 CPU with 16 cores and 256 GB of RAM. Mesh densities were manually set to achieve similar accuracies within *COMSOL Multiphysics*®. The finer meshes had a total of 4,429 and 18,032 tetrahedral elements

TABLE 3. Fabry-Perot resonance simulation results with numerical modeling M5.

Parameter at ω_{fp}		Sample #1	Sample #2
M5: Numerical (Finite-element) Modeling using *COMSOL Multiphysics*® (Using measured f_{fp}, $\lvert S_{21}\rvert$)	ε'_{reff}	2.3284 (2.3270)	2.3080 (2.3061)
	$tan\delta_e \times 10^4$	19.148 (19.148)	14.798 (14.798)
	f_{fp} [GHz]	11.080	11.130
	$\lvert S_{11}\rvert$ [dB]	-53.2565 (-52.4620)	-55.4752 (-54.3515)
	$\lvert S_{21}\rvert$ [dB]	-0.03800 (-0.03811)	-0.02980 (-0.02990)
	τ_g [ps]	61.405 (61.514)	60.942 (61.045)
	Q_U	489.2 (489.1)	621.2 (621.1)
	Q_e	2.146 (2.150)	2.138 (2.142)
	Q_L	2.137 (2.141)	2.131 (2.135)
Analytical modeling with field integrals calculated from analytical expressions for the EM fields (Using f_{fp}, ε'_{reff} and $tan\delta_e$ from M5)	Q_c	8008.6 (8066.0)	8027.5 (8084.0)
	Q_d	521.4 (517.90)	674.65 (670.20)
	Q_U	489.53 (486.70)	622.35 (618.90)
	Q_e	2.1501 (2.1868)	2.1436 (2.1798)
	Q_L	2.1407 (2.1770)	2.1362 (2.1722)
Analytical modeling with field integrals computed within *COMSOL Multiphysics*® from finite-element simulations of EM fields (Using f_{fp}, ε'_{reff} and $tan\delta_e$ from M5)	Q_c	7494.6 (7515.0)	7511.9 (7532.0)
	Q_d	522.04 (522.22)	675.50 (675.70)
	Q_U	488.04 (488.30)	619.76 (620.10)
	Q_e	2.1171 (1.8425)	2.1105 (1.8250)
	Q_L	2.1079 (1.8356)	2.1034 (1.8370)

(respectively, taking 24 and 54 minutes to simulate), for the first and second approaches, respectively. The results from both approaches are shown in TABLE 3 (second approach values in brackets), giving very similar results.

When compared to analytical modeling, the return losses are slightly different; attributed to a non-zero mesh resolution. As expected, the differential-phase group delay and associated Q-factors are the same as those found with analytical (*variational*) modeling M1.

In summary, with numerical Fabry-Pérot resonance modeling M5, the extracted sample average fitted dielectric constant and loss tangent for our ABS are 2.32 and 17×10^{-4}, respectively, at 11.1 GHz.

F. FABRY-PÉROT RESONANCE MODELING RESULTS

The fitted dielectric properties for Samples #1 and #2 extracted from the independent analytical (*variational*), equivalent circuit (distributed-element) and numerical (finite-element) Fabry-Pérot resonance modeling strategies M1, M3 and M5, respectively, agree with one another at the Fabry-Pérot resonance frequencies.

FIGURE 6 shows the measured and simulation frequency responses using the extracted results from the analytical M1 and numerical M5 modeling strategies.

Excellent fits are found for the insertion loss across the whole of X-band. Therefore, a number of important conclusions can be made: (i) the analytical approach adopted here gives effectively the same results as the numerical approach, with only 0.15% and 0.53% discrepancies in the independently extracted dielectric constants and loss tangents; (ii) Fabry-Pérot resonance modeling, matching just the insertion loss at only the single Fabry-Pérot resonances target frequency, fits across the whole of X-band, validating our original statement that the dielectric properties of our FDM 3-D printed ABS samples are not frequency dispersive; (iii) from this simple extraction process for our FDM 3-D printed ABS Samples #1 and #2, the dielectric constant and loss tangent are approximately 2.3 and $< 20\times10^{-4}$, respectively, validating our original low loss findings [3] and contradicting the previously reported results for FDM 3-D printed ABS [17].

IV. ANALYTICAL FIELD-BASED Q-FACTOR MODELING

The constituent Q-factor contributions associated with Fabry-Pérot resonance have been modeled analytically using an electromagnetic (EM) field-based approach, with its bespoke textbook derivation given in Appendix A. EM field integrals are calculated either using purely analytical expressions for the electric and magnetic field components or computed directly within *COMSOL Multiphysics*® (by defining the surface and volume integrals of the individual field components) from numerical (finite-element) simulations. The results are shown in the lower-half of TABLE 3. As expected, Q-factors predicted using both analytical field-based modeling strategies give consistent results with the numerical modeling approach M5.

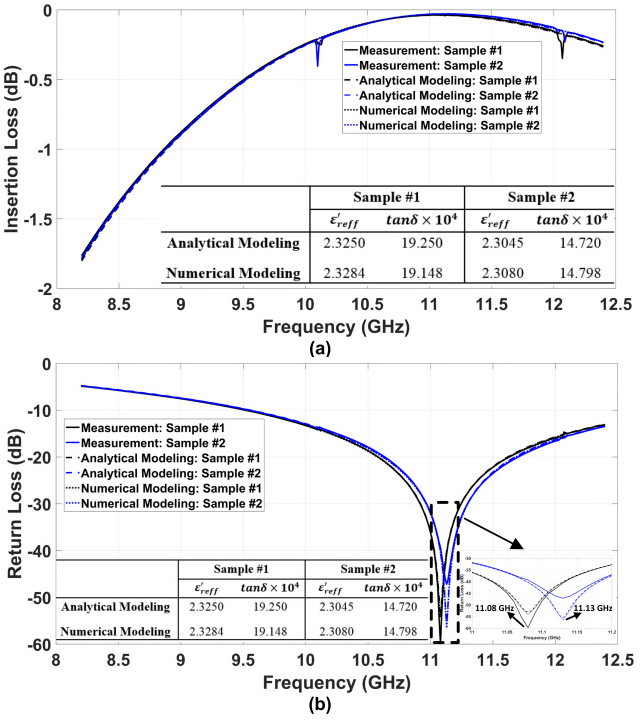

FIGURE 6. Measured and Fabry-Pérot resonance modeled responses for FDM 3-D printed ABS Samples #1 and #2 in standard WR-90 quarter-wavelength thru line waveguide: (a) insertion loss and (b) return loss.

V. OPEN-BOX MODE RESONANCES MODELING

The measured normalized power responses are shown in FIGURE 7 for Samples #1 and #2. It can be seen that both samples give almost identical power responses across the whole of X-band. Any dominant TE or TM traveling-waves propagate through the dielectric-filled MPRWG in the longitudinal direction and, obviously, do not require any form of imperfections/inhomogeneity to excite these modes. In contrast, however, the dielectric-filled MPRWG section also behaves as a parallel-plate dielectric waveguide with short circuits at both ends in the transverse direction; any imperfections/inhomogeneity in the sample excite standing-wave resonant modes, which are confined in the transverse direction. The presence of these *'open-box'* modes are evident by small notches centered at their resonance frequencies, seen in the transmittance and absorptance responses of FIGURE 7.

The dielectric constant and loss tangent values, extracted at the Fabry-Pérot resonance frequency, were adopted from numerical Fabry-Pérot resonance modeling with M5. With finite conductivity waveguide walls, the *COMSOL Multiphysics*® eigenmode solver predicts the complex eigenfrequencies directly. Then, by observing the resulting field patterns (shown in Appendix B for Sample #1), the open-box modes within X-band seen in FIGURE 7 were identified as the TE_{201}, TE_{011} and TE_{111} modes. In addition, from first principles with a PEC-walled waveguide, Appendix B gives a field-based analytical derivation for the open-box mode resonance frequencies.

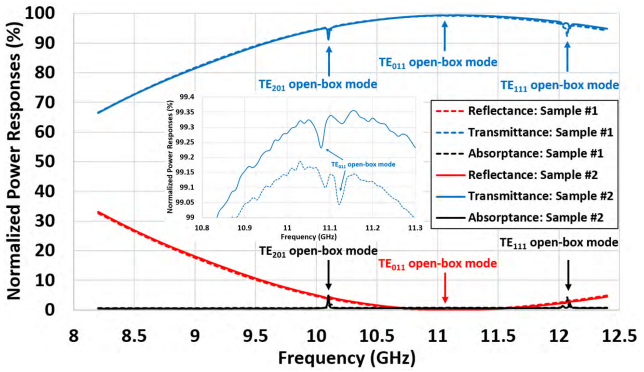

FIGURE 7. Normalized power responses for FDM 3-D printed ABS Samples #1 and #2 filling the standard WR-90 quarter-wavelength thru line waveguide.

TABLE 4. Open-box mode resonance frequencies (and associated mode Q-factors) spectroscopically measured and predicted using numerical eigenmode solver and field-based analytical solutions.

Open-box Mode		TE_{101}	TE_{201}	TE_{011}	TE_{111}
Sample #1 ($\varepsilon'_{reff} = 2.3284, tan\delta = 19.1480 \times 10^{-4}$)					
$\lvert\tilde{f}_{mnp}\rvert$ [GHz]	Measured	-	10.115	11.115	12.065
$\tilde{f}_{mnp}$ ($\lvert\tilde{f}_{mnp}\rvert$) [$Q_u(\lvert\tilde{f}_{mnp}\rvert)$]	Analytical Solution $\rho_o = 0$	5.6065+ j0.0036 (5.607) [778.7]	10.0732+ j0.0084 (10.073) [599.6]	11.1431+ j0.0095 (11.143) [586.5]	12.0450+ j0.0105 (12.045) [573.6]
	Eigenmode Solver $\rho_o = \rho_o\lvert_{brass}$	5.6035+ j0.0078 (5.604) [359.2]	10.074 + j0.005 (10.074) [1007.4]	11.144 + j0.0059 (11.144) [944.4]	12.046 + j0.006 (12.046) [1003.8]
Sample #2 ($\varepsilon'_{reff} = 2.3080, tan\delta = 14.7975 \times 10^{-4}$)					
$\lvert\tilde{f}_{mnp}\rvert$ [GHz]	Measured	-	10.100	11.080	12.090
$\tilde{f}_{mnp}$ ($\lvert\tilde{f}_{mnp}\rvert$) [$Q_u(\lvert\tilde{f}_{mnp}\rvert)$]	Analytical Solution $\rho_o = 0$	5.6229 + j0.0028 (5.623) [1004.1]	10.1118+ j0.0065 (10.112) [777.8]	11.186+ j0.0074 (11.187) [755.9]	12.0931+ j0.0081 (12.093) [746.5]
	Eigenmode Solver $\rho_o = \rho_o\lvert_{brass}$	5.6199 + j0.0068 (5.620) [413.2]	10.113 + j0.0043 (10.113) [1175.9]	11.188 + j0.0044 (11.188) [1271.4]	12.095 + j0.0045 (12.095) [1343.8]

The numerically and analytically predicted open-box mode resonance frequencies for both Samples #1 and #2 are listed in TABLE 4 (giving less than 1% error, when compared to measurements). By inspection of TABLE 4, it can be seen that there is less than 0.02% discrepancy between the results from the numerical (finite-element) eigenmode solver that considers both conductor and dielectric losses and analytical modeling that assumes a PEC-walled waveguide.

VI. SPECTROSCOPIC EXTRACTION OF COMPLEX DIELECTRIC PROPERTIES USING NEW MANUAL 'GRAPHICAL' APPROACH

The new *graphical*-based technique for extracting complex dielectric properties was originally intended for low-cost scalar reflection-transmission mode spectroscopy [1]. In theory, a scalar network analyzer only requires three physical measurements to resolve the ambiguity with multiple solutions possible in $n - \kappa$ space: (i) reflectance, (ii) transmittance; and (iii) reflectance with a PEC backshort (i.e., with $Z_T = 0$ at port-2). However, the third measurement is not physically necessary if a VNA is employed, as it provides both the magnitude and phase information needed to mathematically emulate it; avoiding the introduction of any additional measurement uncertainty.

By mathematically short circuiting the output port of an original two-port S-parameter network, having matrix $[S]$, the S_{11}^{PEC} and resulting PEC reflectance $\mathcal{R}^{PEC}$ from the resulting one-port network (i.e., shorted l-stage, where l represents the thickness of the dielectric-filled material) can be mathematically emulated using the following,

$$S_{11}^{PEC} = S_{11} - \frac{S_{21}S_{12}}{1 + S_{22}} \tag{67}$$

$$\mathcal{R}^{PEC} \equiv \left|S_{11}^{\text{PEC}}\right|^2 \tag{68}$$

The exact complex dielectric properties can then be theoretically extracted by finding the simultaneous solution for the following three equations using our Graphical techniques with ideal measured values [1],

$$|S_{11SIM}(\tilde{n})|^2 - \mathcal{R}_{MEAS} = 0 \tag{69}$$

$$|S_{21SIM}(\tilde{n})|^2 - \mathcal{T}_{MEAS} = 0 \tag{70}$$

$$\left|S_{11SIM}^{\text{PEC}}(\tilde{n})\right|^2 - \mathcal{R}_{MEAS}^{\text{PEC}} = 0 \tag{71}$$

where, $S_{11SIM}(\tilde{n})$, $S_{21SIM}(\tilde{n})$ and $S_{11SIM}^{\text{PEC}}(\tilde{n})$ are analytically simulated variables, all being a function of the extractable complex refractive index $\tilde{n} = n - j\kappa = \sqrt{\tilde{\mu}_r\tilde{\varepsilon}_{reff}}$; optical constants n and κ are the associated index of refraction (or refractive index) and extinction coefficient (or absorption index), respectively [1]; $\mathcal{R}_{MEAS}$ and $\mathcal{T}_{MEAS}$ are the measured reflectance and transmittance for the l-stage network, respectively. To avoid ambiguity, the generalized Q-factor for an unbound dielectric Q_0 is given by,

$$Q_0 = \frac{1}{tan\delta} = \frac{Re\{\tilde{\mu}_r\tilde{\varepsilon}_{reff}\}}{Im\{\tilde{\mu}_r\tilde{\varepsilon}_{reff}\}} = \frac{Re\{\tilde{n}^2\}}{Im\{\tilde{n}^2\}} = \frac{n^2 - \kappa^2}{2n\kappa} \tag{72}$$

This can be broken down into its constituent magnetic and electric components Q_{0m} and Q_{0e}, respectively,

$$Q_0 = \frac{Q_{0m}Q_{0e} - 1}{Q_{0m} + Q_{0e}} \cong Q_{0m} // Q_{0e} \tag{73}$$

where,

$$Q_{0m} = \frac{1}{tan\delta_m} = \frac{\mu'_r}{\mu''_r} \quad \text{and} \quad Q_{0e} = \frac{1}{tan\delta_e} = \frac{\varepsilon'_{reff}}{\varepsilon''_{reff}} \tag{74}$$

With ideal measured values [1], all responses from the l-stage reflectance, transmittance and port-1 reflectance with port-2 short-circuited simultaneously coincide at the true values for n and κ in $n - \kappa$ space. It has been found that (71) is sensitive to measurement noise and so a more resilient Graphical approach is presented here that replaces (71) with alternative constraints. For example, $2l$-stage responses, where two identical S-parameters for the l-stage matrix $[S]$ are cascaded together to create matrix $\left[S^{CAS}\right]$, which emulates a double-length section having S-parameters:

$$S_{11}^{CAS} = S_{11}\left(1 + S_{21}^{CAS}\right) \quad \text{and} \quad S_{21}^{CAS} = \frac{S_{21}^2}{1 - S_{11}^2} \tag{75}$$

$$\mathcal{R}^{CAS} \equiv \left|S_{11}^{CAS}\right|^2 \quad \text{and} \quad \mathcal{T}^{CAS} \equiv \left|S_{21}^{CAS}\right|^2 \tag{76}$$

where, $\mathcal{R}^{CAS}$ and $\mathcal{T}^{CAS}$ are the reflectance and transmittance for the $2l$-stage cascaded network, respectively.

Therefore, the complex refractive index can be extracted by simultaneously solving the following equations for $2l$-stage responses in addition to (69)-(70) for the l-stage,

$$\left|S_{11SIM}^{CAS}(\tilde{n})\right|^2 - \mathcal{R}_{MEAS}^{CAS} = 0 \tag{77}$$

$$\left|S_{21SIM}^{CAS}(\tilde{n})\right|^2 - \mathcal{T}_{MEAS}^{CAS} = 0 \tag{78}$$

Similarly, it is also possible to emulate the half-length section (i.e., $l/2$-stage) S-parameters from the following:

$$S_{11}^{HALF} = \frac{S_{11}}{1+S_{21}} \quad \text{and} \quad S_{21}^{HALF} = \sqrt{S_{21}\left[1-\left(\frac{S_{11}}{1+S_{21}}\right)^2\right]} \tag{79}$$

Obviously, by inserting the S-parameters from the resulting matrix $\left[S^{HALF}\right]$ from (79) into (75) for matrix $\left[S^{CAS}\right]$ recovers the original matrix $[S]$. Now,

$$\mathcal{R}^{HALF} \equiv \left|S_{11}^{HALF}\right|^2 \quad \text{and} \quad \mathcal{T}^{HALF} \equiv \left|S_{21}^{HALF}\right|^2 \tag{80}$$

where, $\mathcal{R}^{HALF}$ and $\mathcal{T}^{HALF}$ are the respective reflectance and transmittance for the $l/2$-stage cascaded network.

Therefore, in principle, the complex refractive index can be extracted by simultaneously solving the following equations for the $l/2$-stage responses in addition to (69)-(70) for the l-stage and (77)-(78) for the $2l$-stage,

$$\left|S_{11SIM}^{HALF}(\tilde{n})\right|^2 - \mathcal{R}_{MEAS}^{HALF} = 0 \tag{81}$$

$$\left|S_{21SIM}^{HALF}(\tilde{n})\right|^2 - \mathcal{T}_{MEAS}^{HALF} = 0 \tag{82}$$

It has been found that in $n-\kappa$ space the intersection points of the reflectance and transmittance curves for the $l/2$-stage can be used to give the extracted values for n and κ, to a good approximation, with ideal measured values. Indeed, even at the Fabry-Pérot resonance frequency (with $S_{11}(\omega_{fp}) \cong 0$ and $S_{21}(\omega_{fp}) \cong -1$ for low loss samples), singularities are not seen in (79), as $S_{11}(\omega_{fp}) / (1 + S_{21}(\omega_{fp})) = \lim_{a\to 0}\{a\}/\lim_{b\to 0}\{b\}$. However, this is not the case with real measured values, where the singularity is evident, due to the extreme sensitivity of the denominator to noise in the measured $S_{21}(\omega_{fp})$. Nevertheless, away from the Fabry-Pérot resonance frequency, $l/2$-stage responses can be used to extract values for n and κ from $n-\kappa$ space.

With our new manual Graphical approach, both optical constants are swept independently and all possible solutions for (69)-(70), (77)-(78) and (81)-(82) plotted, using the MATLAB *'fimplicit'* function [21]. For example, all possible solutions are initially plotted for ideal measured values emulated by arbitrarily choosing a value $\tilde{n}_{ideal} = 1.5248 - \text{j}0.001468$ (this complex refractive index is set equal to $\tilde{n}$(11.08 GHz), corresponding to the respective dielectric constant and loss tangent of 2.325 and 19.26 $\times 10^{-4}$ for Sample #1 at the Fabry-Pérot resonance frequency, as given in TABLE 1, associated with Fabry-Pérot resonance modeling with the *variational* method). FIGURES 8(a), 9(a) and 10(a) show the individual solutions in $n-\kappa$ space at the respective arbitrarily chosen frequencies of 8.2, 11.08 and 12.4 GHz with a noiseless scenario. The individual solutions for (69)-(70), (77)-(78) and (81)-(82) are represented by the respective solid red-blue, dashed red-blue and dotted red-blue curves. As expected, the $l/2$-stage, l-stage and $2l$-stage reflectance and transmittance curves all have the same intersection point and, thus, it is easy to manually extract the dielectric properties without ambiguity using the Graphical approach within a noiseless scenario. Here, the original dielectric properties are recovered without error.

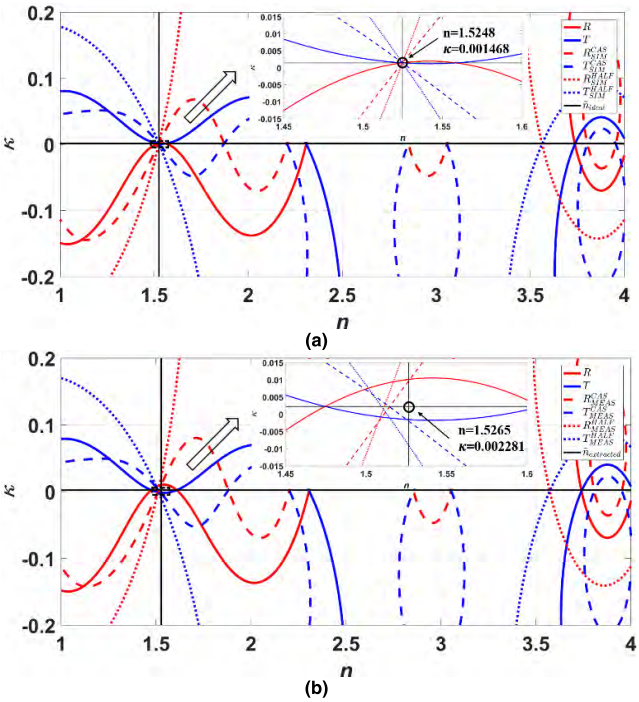

FIGURE 8. Individual solutions in $n-\kappa$ space at 8.2 GHz from (a) ideal noiseless measurements emulated with $\tilde{n}_{ideal} = 1.5248 - j0.001468$ (set equal to $\tilde{n}$(11.08 GHz) from Sample #1 associated with Fabry-Pérot resonance modeling with the *variational* method); and (b) real noisy measurements for Sample #1, having $\tilde{n}_{extracted} = 1.5265 - j0.002281$ (corresponding to a dielectric constant and loss tangent of 2.330 and 29.89 $\times$ 10^{-4}, respectively).

With real noisy measurements, a practical Graphical approach avoids the use of the sensitive shorted l-stage network with (71) and potentially unstable $l/2$-stage network with (81)-(82). Instead, values of n and κ can be extracted from $n-\kappa$ space with just the l-stage and $2l$-stage networks, using the following graphical rules:

(i) the intersection point from the l-stage and $2l$-stage reflectance curves and also that from the transmittance curves separate in $n-\kappa$ space when noise is introduced; creating an interval Δn in the n-direction. Within the lowest observable Δn interval, to a good approximation, our extracted value of n is the mean value between

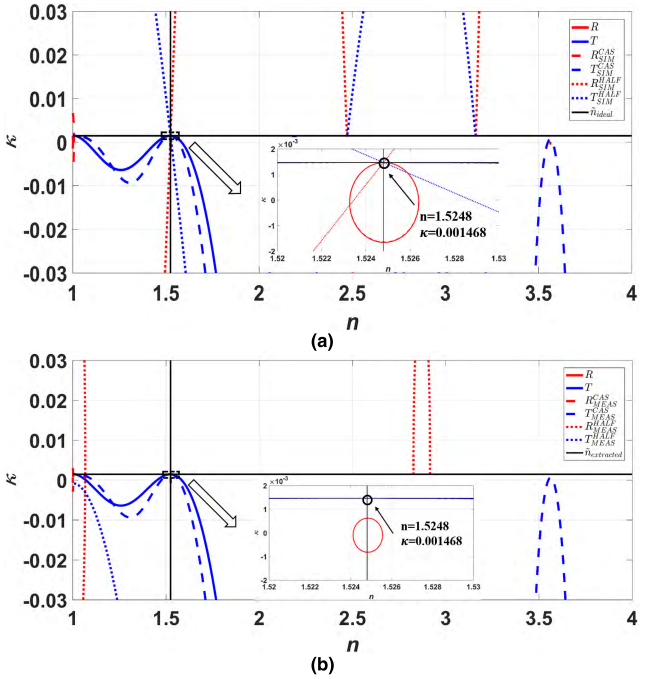

FIGURE 9. Individual solutions in $n-\kappa$ space at 11.08 GHz from (a) ideal noiseless measurements emulated with $\tilde{n}_{ideal} = 1.5248 - j0.001468$ (set equal to $\tilde{n}$(11.08 GHz) from Sample #1 associated with Fabry-Pérot resonance modeling with the *variational* method); and (b) real noisy measurements for Sample #1, having $\tilde{n}_{extracted} = 1.5248 - j0.001468$ (corresponding to a dielectric constant and loss tangent of 2.325 and 19.26×10^{-4}, respectively).

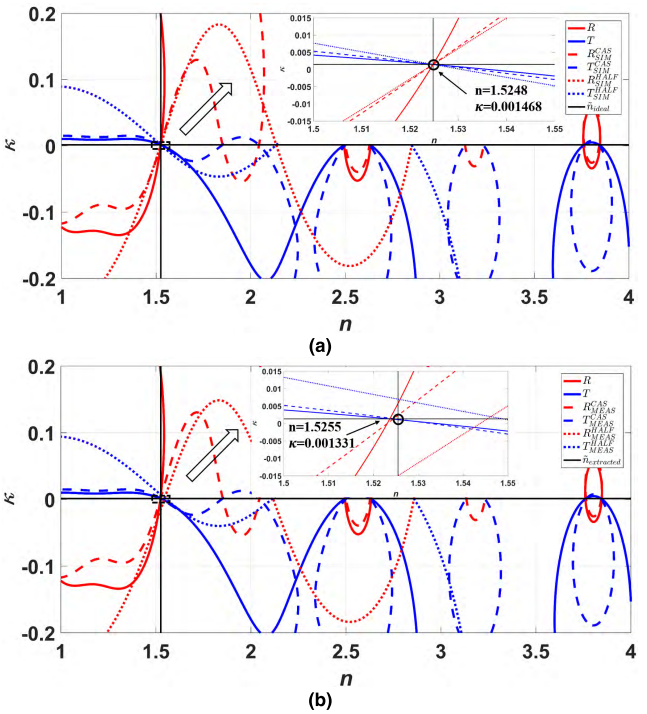

FIGURE 10. Individual solutions in $n-\kappa$ space at 12.4 GHz from (a) ideal noiseless measurements emulated with $\tilde{n}_{ideal} = 1.5248 - j0.001468$ (set equal to $\tilde{n}$(11.08 GHz) from Sample #1 associated with Fabry-Pérot resonance modeling with the *variational* method); and (b) real noisy measurements for Sample #1, having $\tilde{n}_{extracted} = 1.5255 - j0.001331$ (corresponding to a dielectric constant and loss tangent of 2.327 and 17.45×10^{-4}, respectively).

the two intersection points – both intersection points are considered to be independent of the true value of κ with real noisy measurements.

(ii) to a good approximation, the extracted value of κ is the repeated intersection points of reflectance and transmittance for the l-stage – these intersection points are considered to be independent of the true value of n with real noisy measurements. One exception to this rule is when there is no interception (e.g., at the Fabry-Pérot resonance frequency); in this case the extracted value of κ is the peak value of the l-stage transmittance curve found at the extracted value of n. Another exception is at the open-box mode resonance frequencies, where the extracted value of κ is artificially too high; it is an artifact of the resonant structure and does not represent the intrinsic loss of the sample under test. As a result, extracted values for κ should be discounted at the open-box mode resonance frequencies.

For example, all possible solutions are plotted using the real noisy measurements for Sample #1. FIGURES 8(b), 9(b) and 10(b) show the individual solutions in $n-\kappa$ space at the respective arbitrarily chosen frequencies of 8.2, 11.08 and 12.4 GHz. Here, using the above rules, the extracted dielectric properties are very close to those extracted using the independent Fabry-Pérot resonance modeling at 8.2 and 12.4 GHz and, as expected, exactly the same at 11.08 GHz.

Across X-band, from these three spectroscopic measurements, the dielectric constant varies between 2.325 and 2.330, corresponding to a variation of only $\pm 0.1\%$, while the loss tangent decreases from 29.89×10^{-4} down to 17.45×10^{-4} as frequency increases. These trends are investigated with finer frequency resolution in Section VIII.

Using our new manual Graphical approach, the extracted values of dielectric constant and loss tangent for both Samples #1 and #2 are shown in FIGURE 11, covering the whole of X-band (in 0.1 GHz steps). Note that the data points at 10.1 GHz and 12.1 GHz, associated with the open-box mode resonances (seen in FIGURE 7), have been included even though they represent errors for an unbound dielectric.

Our Graphical technique is immune to the effects of the Fabry-Pérot resonances (not seen in FIGURE 7). It is interesting to note that both the dielectric constant and loss tangent for Sample #1 are marginally larger in value than those for Sample #2, which is consistent with all the earlier results found with Fabry-Pérot resonance modeling.

VII. SPECTROSCOPIC EXTRACTION OF COMPLEX DIELECTRIC PROPERTIES USING NEW AUTOMATED 'RENORMALIZATION' METHOD

With ideal measured values, at each individual frequency, the simultaneous complex root solutions to (69)-(71) give the ideal complex refractive index $\tilde{n}_{ideal}$, seen as a single

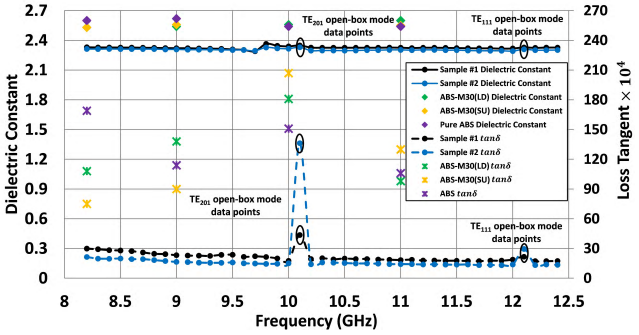

FIGURE 11. Extracted values for dielectric constant and loss tangent (in 0.1 GHz steps) using the manual Graphical approach with *l*- and 2*l*-stages for Samples #1 and #2.

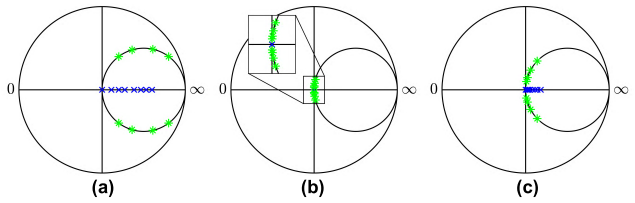

FIGURE 12. Port reference impedances plotted on impedance Smith chart normalized to $Z^{air}_{TE10}(\omega)$ for Sample #1. Blue crosses represent purely real impedances, while green asterisks represent complex impedances on the $1 \pm jx$ circle: (a) 8.2 GHz; (b) 11.08 GHz; (c) 12.4 GHz.

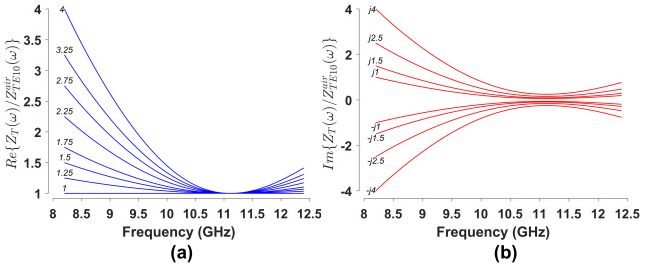

FIGURE 13. Port reference impedance plotted against frequency normalized to $Z^{air}_{TE10}(\omega)$ for Sample #1, corresponding to the recommended data set: (a) $Re\left\{Z_T(\omega)/Z^{air}_{TE10}(\omega)\right\}$ corresponding to the $r \pm j0$ line; (b) $Im\left\{Z_T(\omega)/Z^{air}_{TE10}(\omega)\right\}$ corresponding to the $1 \pm jx$ circle.

intersection point in $n-\kappa$ space. However, as previously seen, with real, noisy, measurements there is no longer a single intersection point. By scanning $n-\kappa$ space, the magnitudes of the right-hand sides of (69)-(71) can be summed and projected onto a contour plot. As a result, with ideal measured values there will be a single one-dimensional spike in $n-\kappa$ space, touching zero at the simultaneous solution; while with real, noise-affected, measurements a three-dimensional spike will approach zero. In practice, the contour plot can be best observed on a logarithmic scale, by first subtracting the minimum value and then dividing throughout by the maximum value (giving normalized values between 0 and 1). At some frequencies there may be multiple intersection points in $n-\kappa$ space that result in multiple minima. The dominant minimum in this case might correspond to incorrect values for n and κ.

Adding more equations (increasing sensitivity) and including more constraints to the existing equations (increasing robustness) lead to a sharper spike at the correct simultaneous solution in $n-\kappa$ space. The former can be implemented by mathematically introducing additional sub- and multiple-stages (e.g., $l/2$-stage and $2l$-stage) to the original l-stage and shorted l-stage. The latter can employ port reference impedance renormalization. While spurious minima are generated, the correct solution will have the dominant (deepest) spike. This is because, with impedance renormalization, the correct intersections will remain fixed in $n-\kappa$ space, while spurious intersections move around and are subsequently averaged-out on aggregate. Spurious spikes can be removed by: (i) increasing grid resolution (thereby reducing discretization error); (ii) introducing more sub- or multiple-stages; (iii) choosing a different port reference impedance renormalization set.

As a general rule-of-thumb, in addition to the original S-parameters (i.e., l-stage having $Z_T(\omega) = Z^{air}_{TE10}(\omega)$, calculated using (30)) it has been found that the best selection of renormalization impedances includes several purely resistive impedances above $Z^{air}_{TE10}(\omega)$ (sharpening the spike in the κ-direction) and introducing an equal number of positive and negative reactances (sharpening the spike in the n-direction). It has been found that at the Fabry-Pérot resonance frequency, the method is very sensitive. As a result, the port reference impedances should be close to $Z^{air}_{TE10}(\omega)$ at the Fabry-Pérot resonance frequency, while spreading out more from $Z^{air}_{TE10}(\omega)$ when moving further from the Fabry-Pérot resonance frequency. A good implementation has a spread of port reference impedances with $r = Re\left\{Z_T(\omega)/Z^{air}_{TE10}(\omega)\right\} \in [1, 4]$ and $x = Im\left\{Z_T(\omega)/Z^{air}_{TE10}(\omega)\right\} \in [-4, 4]$. As a good example, when normalized to $Z^{air}_{TE10}(\omega)$, one can adopt the following recommended port reference impedance set: $Z_T(\omega)/Z^{air}_{TE10}(\omega) \in \left[1, 1.25, 1.5, 1.75, 2.25, 2.75, 3.25, 4, 1 \pm j1, 1 \pm j1.5, 1 \pm j2.5, 1 \pm j4\right]$ used at all frequencies; purely real port reference impedances lie on the $r \pm j0$ line above unity, while complex impedances lie on the $1 \pm jx$ circle. This dynamic spread is shown in the Smith chart illustrations of FIGURE 12(a) at 8.2. GHz, with FIGURE 12(b) at the Fabry-Pérot resonance frequency and FIGURE 12(c) at 12.4 GHz. FIGURE 13 shows port reference impedances as a function of frequency with $|S_{11SIM}|^2$ used as a scaling function. The choice of port reference impedance renormalization set is flexible (in terms of size and values), which can change with frequency and/or measurement conditions.

This measurement post-processing technique can be fully automated, as demonstrated in this section for all the frequency points generated by the VNA. As an implementation consideration, there may be a practical limit on the discretization of $n-\kappa$ space, in terms of computational time and memory storage. The optimal approach is to first run coarse discretization over a wide $n-\kappa$ space, followed by finer discretization over a reduced $n-\kappa$ space centered on the expected value.

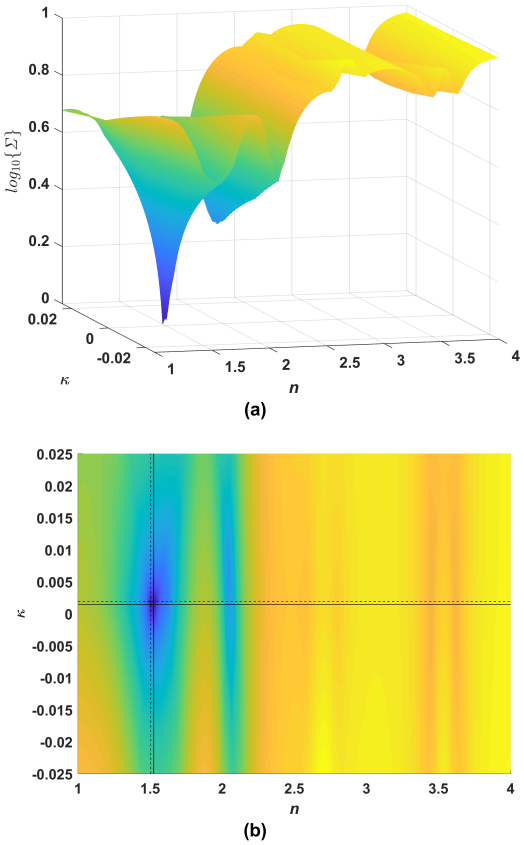

FIGURE 14. Contour plots for common log of summations of the right-hand sides for (69)-(71), (77)-(78) and (81)-(82) for Sample #1 at 9 GHz without renormalization: (a) side view; (b) top view with solid black lines showing the target value $\tilde{n}$(11.08 GHz) and dotted black lines showing the extracted value.

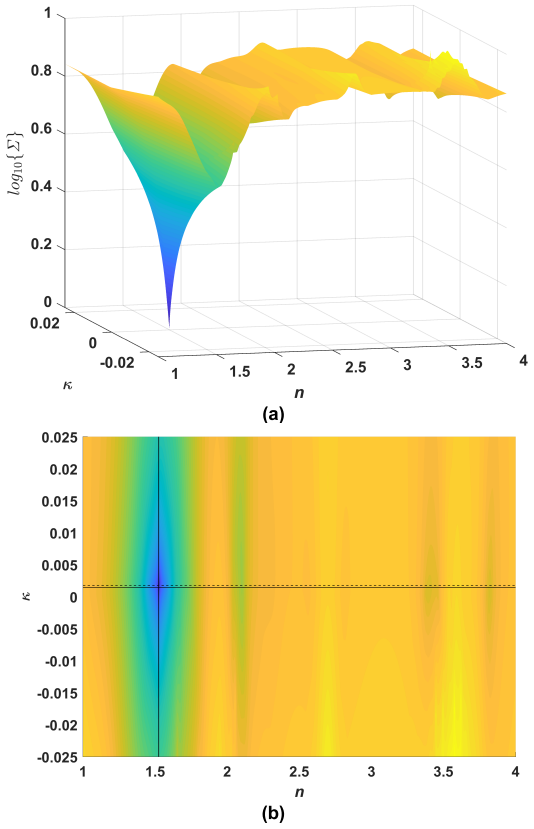

FIGURE 15. Contour plots for common log of summations of the right-hand sides of (69)-(71), (77)-(78) and (81)-(82) for Sample #1 at 9 GHz with renormalization: (a) side view; (b) top view with solid black lines showing the target value $\tilde{n}$(11.08 GHz) and dotted black lines showing the extracted value.

With the previously recommended port reference impedance renormalization set, dielectric properties were automatically extracted. Coarse discretization had $n \in [1, 4]$ and $k \in [-0.025, 0.025]$ and the finer discretization had $n \in [1.5, 1.55]$ and $\kappa \in [0, 0.009]$, while grid size was kept at 1000^2 for both runs. With the latter, contour plots have less spikes that allow for easy identification of $\tilde{n}_{extracted}$.

The former gives the worst-case condition. For example, contour plots with coarse discretization are shown for Sample #1 at 9 GHz, without impedance renormalization in FIGURE 14 and with impedance renormalization in FIGURE 15, where both figures represent the common log of the summation Σ of (69)-(71), (77)-(78) and (81)-(82). The solid black lines in FIGURE 14(b) and FIGURE 15(b) correspond to $\tilde{n}$(11.08 GHz) for Sample #1 associated with Fabry-Pérot resonance modeling with the *variational* method M1, while the dashed black lines show the location of absolute minimum (extracted value). As expected, without impedance renormalization there are multiple minima; while the contour plot with impedance renormalization shows that the deepest spike corresponds to the absolute minimum close to $\tilde{n}$(11.08 GHz) and other spikes are suppressed.

The spectroscopic results from all frequency points generated by the VNA (in 0.01 GHz steps) are shown in FIGURE 16(a) without impedance renormalization and in FIGURE 16(b) with impedance renormalization. The effect of absorption due to box modes can be seen as sharp spikes in the extracted values of loss tangent. Clearly, impedance renormalization gives the expected dielectric properties.

VIII. MODELING COMPARISON WITH NICOLSON-ROSS-WEIR (NRW) APPROACH

Values of dielectric constant and loss tangent for ABS (pure ABS and two FDM 3-D printed Stratasys ABS-M30 samples in 'laying down' (LD) and 'standing up' (SU) orientations), extracted using the Nicolson-Ross-Weir (NRW) approach, have been published in the open literature by Deffenbaugh *et al.* [17], having a sample size of $22.60 \times 10.06 \times 7.63$ mm^3; all the available X-band data is included in FIGURE 11 and TABLE 5. TRL calibration was also employed before measurements and their samples were similarly made to fit a shorter 7.63 mm long air-filled quarter-wavelength thru line section of WR-90 waveguide [17]. Their sample length resulted in Fabry-Pérot resonances above *ca.* 11 GHz [17]; with f_{fp} ~13 GHz, predicted using (27), having broader spectral features (due to their much greater loss tangents). It can be seen from the published data (recorded at only 8.2, 9.0, 10.0 and 11.0 GHz),

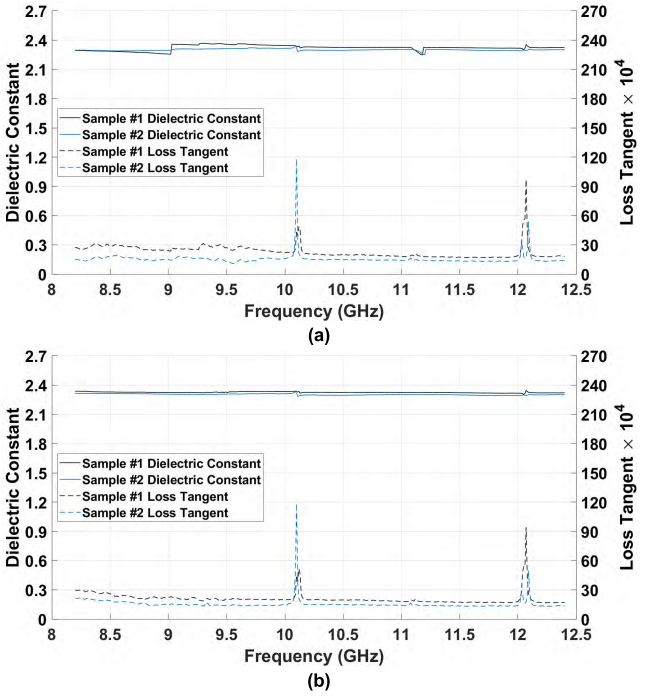

FIGURE 16. Extracted values for dielectric constant and loss tangent (in 0.01 GHz steps) using automated Renormalization techniques with *l*/2-, *l*-, 2*l*-stages and shorted *l*-stage: (a) without impedance renormalization; and (b) with impedance renormalization.

TABLE 5. NRW extracted X-band dielectric properties for all ABS samples reported by Deffenbaugh *et al.* [17].

Dielectric Property	Spot Frequencies [GHz]				
	8.20	9.00	10.00	11.00	12.40
Pure ABS					
Dielectric Constant	2.6	2.62	2.54	2.54	-
Loss Tangent × 10^4	169	114	151	106	-
ABS-M30(LD)					
Dielectric Constant	2.53	2.54	2.56	2.6	-
Loss Tangent × 10^4	108	138	181	98	-
ABS-M30(SU)					
Dielectric Constant	2.53	2.56	2.54	2.55	-
Loss Tangent × 10^4	75	90	207	130	-

their ABS samples have an extracted dielectric constant of between 2.53 and 2.62; higher than our extracted values. Moreover, the associated loss tangents vary from 75×10^{-4} to 207×10^{-4} (extreme case for ABS-M30(SU)); considerably more lossy than our FDM 3-D printed ABS Samples #1 and #2.

It is worth noting that Deffenbaugh *et al.* also present extracted dielectric constant data, using non-waveguide techniques, for ABS at 1, 2, 100, 500 and 1,000 MHz; giving values ranging from 2.59 to 2.83, which correspond more closely to their fixed data sheet value of 2.8 for all ABS samples [17].

The well-established NRW approach [22], [23] represents a closed-form analytical method for characterizing dielectric and magnetic materials, without using iterations and an initial guess. The original, highly cited, paper by Nicolson and Ross was developed for TEM waves, normally associated with coaxial cables [22] (it is not possible to 3-D print truly cylindrical samples with FDM for this application). However, it has also been used with TE and TM modes normally associated with waveguides [17], [23]–[26]. For the purposes of clarity, this approach is referred to here as the Original NRW approach.

Given the dielectric properties, *a priori*, the S-parameters for any medium can be calculated using [1],

$$S_{11} = \left[\frac{1-P^2}{1-(\rho_0 P)^2}\right]\rho_0 \equiv S_{22} \tag{83}$$

$$S_{21} = \left[\frac{1-\rho_0^2}{1-(\rho_0 P)^2}\right]P \equiv S_{12} \tag{84}$$

where, using (6) for Z_{TEm0} and Z^{air}_{TEm0}, the zero-order electric-field wave (or complex Fresnel) reflection coefficient ρ_0 at the interface between the reference air-filled and sample dielectric-filled sections of a MPRWG is,

$$\rho_0 = \frac{Z_{TEm0} - Z^{air}_{TEm0}}{Z_{TEm0} + Z^{air}_{TEm0}} \tag{85}$$

and, using (1) for γ_{m0}, the propagation factor $P = e^{-\gamma_{m0} l}$. Here, the propagation constant $\gamma_{m0} \rightarrow \gamma_g = j\tilde{\beta}$, using (25) for $\tilde{\beta}$; this implicitly assumes a PEC-walled MPRWG.

Now, the reverse process of extracting the dielectric properties from any medium can be performed. For example using a dielectric slab in free space [1], coaxial cable [22] and rectangular waveguide [17], [23]–[26], by solving the following quadratic function,

$$\rho_o^2 - 2\chi\rho_o + 1 = 0 \tag{86}$$

giving,

$$\rho_o = \frac{\xi - 1}{\xi + 1} \equiv \chi \pm \sqrt{\chi^2 - 1}$$

where

$$\chi = \frac{1 - S_{21}^2 + S_{11}^2}{2S_{11}} \tag{87}$$

The complex propagation factor $P = e^{-j2\pi l/\tilde{\lambda}_g}$ can now be found directly from measurements with (87) using,

$$P = \frac{S_{11} + S_{21} - \rho_0}{1 - (S_{11} + S_{21})\rho_0} \tag{88}$$

In principle, the complex relative effective permittivity $\tilde{\varepsilon}_{reff}$ and permeability $\tilde{\mu}_r$ can be extracted using (19)-(22),

$$\frac{1}{\tilde{\lambda}_g^2} = -\left[\frac{ln\{P\}}{2\pi l}\right]^2 = \left(\frac{\tilde{\mu}_r\tilde{\varepsilon}_{reff}}{\lambda_0^2} - \frac{1}{\lambda_{cm0}^2}\right) \tag{89}$$

Rearranging (89) gives,

$$\tilde{\varepsilon}_{reff} = \frac{\lambda_0^2}{\tilde{\mu}_r}\left(\frac{1}{\tilde{\lambda}_g^2} + \frac{1}{\lambda_{cm0}^2}\right) \tag{90}$$

where, with (7) and the general identities in (16),

$$\tilde{\mu}_r = \xi \cdot \frac{\lambda_g^{air}}{\tilde{\lambda}_g} \tag{91}$$

and,

$$\xi = \frac{1+\rho_0}{1-\rho_0} \quad \text{and} \quad \lambda_g^{air} = \lambda_0 \frac{Z_{TE}^{air}}{\eta_0} \tag{92}$$

In practice, the VNA measures S-parameters with wrapped phase angles (i.e., with values limited between $-\pi$ and $+\pi$); the resulting phase ambiguities in P lead to an infinite number of roots when evaluating $ln\{P\}$ in (89) [23]. In practice (with finite $Q_0(f_{fp})$), the effects of the Fabry-Pérot resonances excludes practical extraction of the dielectric properties above *ca.* 10.5 GHz for Sample #1 and above *ca.* 10.75 GHz for Sample #2; the latter exhibiting a higher $Q_0(f_{fp})$. Fortunately, phase correction can be applied to the propagation factor (i.e., adding integer multiples n_φ of 2π to $-\beta l$ by multiplying P in (88) by $e^{+jn_\varphi 2\pi}$) between the n_φ and $n_\varphi + 1$ Fabry-Pérot resonance frequencies [25], [26].

Our measured S-parameters were applied to these NRW equations, using (87)-(92), with phase correction applied, and the extracted relative (effective permittivity and permeability) values are shown in FIGURE 17. This methodology is referred to in this paper as the Original NRW approach.

In addition to the problem of phase ambiguity, there is also an issue with mathematical instability. With ideal measurements, at the Fabry-Pérot resonance frequency (with $S_{11}(\omega_{fp}) \cong 0$ and $S_{21}(\omega_{fp}) \cong -1$ for low loss samples), singularities are not seen in (87), as $\chi = \lim_{a\to 0}\{a\}/\lim_{b\to 0}\{b\}$. However, with real measured values, a singularity propagates from (87) to the propagation factor, resulting in the mathematical instability in both $\tilde{\mu}_r$ and $\tilde{\varepsilon}_{reff}$. In 2012, Barroso and de Paula reported a way to minimize the instability, considering the product of relative effective permeability and relative permittivity [26]; $Re\{\tilde{\mu}_r\tilde{\varepsilon}_{reff}\} = \mu'_r\varepsilon'_{reff} - \mu''_r\varepsilon''_{reff}$ and $Im\{\tilde{\mu}_r\tilde{\varepsilon}_{reff}\} = \mu'_r\varepsilon''_{reff} + \mu''_r\varepsilon'_{reff}$ and $\tilde{\mu}_r$ constrained to a value of unity (restricting this technique to purely non-magnetic materials). This methodology is referred to in this paper as the Modified NRW approach. Here, it is implicitly assumed throughout that phase correction has been applied. Extracted values of $\tilde{\mu}_r\tilde{\varepsilon}_{reff}$, for both samples, are also shown in FIGURE 17, where dielectric constant $\varepsilon'_{reff} = Re\{\tilde{\mu}_r\tilde{\varepsilon}_{reff}\}|_{\tilde{\mu}_r=1}$ is replaced with $Re\{\tilde{\mu}_r\tilde{\varepsilon}_{reff}\}$ and loss tangent $tan\delta_e = tan\delta|_{\mu''_r=0} = \varepsilon''_{reff}/\varepsilon'_{reff}$ replaced with $tan\delta = Im\{\tilde{\mu}_r\tilde{\varepsilon}_{reff}\}/Re\{\tilde{\mu}_r\tilde{\varepsilon}_{reff}\}$.

It is important to note that the extraction of dielectric property for rectangular waveguides using (87)-(92), as originally proposed by Weir [23] and later adopted by others [17], [24]–[26], implicitly assumes PEC-walled MPRWGs. Therefore, with our practical measurements having waveguides with finite conductivity metal walls ($\sigma_o \approx 1.6 \times 10^7$ S/m), extraction using the NRW equations must exhibit errors (a detailed analysis of the impact of finite σ_o on $\tilde{\varepsilon}_{reff}$ and $\tilde{\mu}_r$ is beyond the scope of this paper).

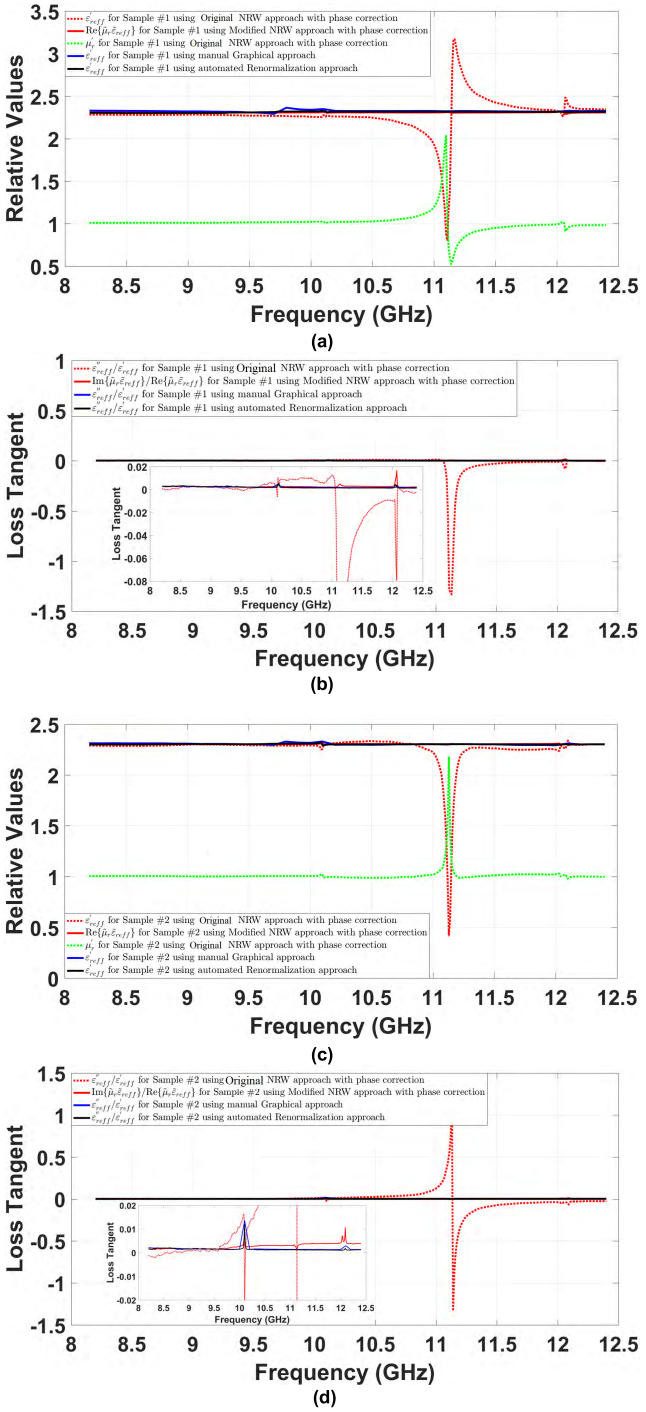

FIGURE 17. Extracted relative (effective permittivity and permeability) values using the Nicolson-Ross-Weir (in 0.01 GHz steps), manual Graphical and automated Renormalization approaches: (a) real part of relative values for Sample #1; (b) loss tangent for Sample #1; (c) real part of relative values for Sample #2; and (d) loss tangent for Sample #2.

It can be seen from FIGURE 17 that, with the Original NRW approach, the extracted relative values and loss tangent exhibit mathematical instabilities at the Fabry-Pérot resonance frequencies ($f_{fp} = 11.08$ GHz for Sample #1 and $f_{fp} = 11.13$ GHz for Sample #2) with $\tilde{\varepsilon}_{reff} \not\equiv \tilde{\mu}_r\tilde{\varepsilon}_{reff}\big|_{\tilde{\mu}_r=1}$.

For this reason, with the Original NRW approach, sample length must be constrained to $l < \lambda_g(f_{fp})/2$ (i.e., so that $\beta(\omega)\, l < \pi$) increasing measurement uncertainly due to low opacity [1], [23]. For example, with our Graphical approach, the extracted value of $\varepsilon'_{reff}(11\text{ GHz}) = 2.3256$ for Sample #1, and so the maximum length $l_{max}(11\text{ GHz}) = 9.708$ mm. As expected, this just exceeds $l = 9.626$ mm, in theory (for $Q_0(f_{fp}) \to \infty$), allowing extraction of dielectric properties below *ca.* 11 GHz only. For arbitrary lengths, one way to resolve the phase ambiguities in P is to test for spectral continuity in the differential-phase group delay [22].

In general, mathematical instabilities are not observed with the Modified NRW method. However, it was found that with Sample #2 an instability was evident just above f_{fp}, where loss tangent spiked to a small negative value.

As seen in FIGURE 17 (ignoring box-mode resonances), the Modified NRW approach gives $Re\{\tilde{\mu}_r\tilde{\varepsilon}_{reff}\} = 2.3080 \pm 0.0019(\pm 0.1\%$ variation), while our respective Graphical and Renormalization approaches give $\varepsilon'_{reff} = 2.3273 \pm 0.0366(\pm 1.6\%$ variation; this relatively large value may be due to systematic errors and noise in the measurements) and $2.3281 \pm 0.0105(\pm 0.4\%$ variation) across X-band for Sample #1; for Sample #2, the Modified NRW approach gives $Re\{\tilde{\mu}_r\tilde{\varepsilon}_{reff}\} = 2.3030 \pm 0.0035(\pm 0.2\%$ variation), while our respective Graphical and Renormalization approaches give $\varepsilon'_{reff} = 2.3105 \pm 0.0183(\pm 0.8\%$ variation) and $2.3047 \pm 0.0119(\pm 0.5\%$ variation) across X-band.

Similarly, with loss tangent across X-band, the Modified NRW approach gives $Im\{\tilde{\mu}_r\tilde{\varepsilon}_{reff}\}/Re\{\tilde{\mu}_r\tilde{\varepsilon}_{reff}\}$ between 18.861×10^{-4} and 31.58×10^{-4}, while our respective Graphical and Renormalization approaches give $\varepsilon''_{reff}/\varepsilon'_{reff}$ from 17.227×10^{-4} to 29.885×10^{-4} and 16.675×10^{-4} to 29.693×10^{-4} for Sample #1. For Sample #2, the Modified NRW approach gives $Im\{\tilde{\mu}_r\tilde{\varepsilon}_{reff}\}/Re\{\tilde{\mu}_r\tilde{\varepsilon}_{reff}\}$ between 13.514×10^{-4} and 48.97×10^{-4}, while our respective Graphical and Renormalization approaches give $\varepsilon''_{reff}/\varepsilon'_{reff}$ from 13.195×10^{-4} to 21.473×10^{-4} and 12.948×10^{-4} to 21.429×10^{-4}.

A summary of the dielectric properties for ABS extracted using various strategies is shown in TABLE 6, for both Samples #1 and #2. It can be seen that at the Fabry-Pérot resonance frequencies the extracted dielectric constants are consistent amongst the various extraction strategies, with the exception of the two NRW methods. The Original NRW method is not stable at this frequency and so generates wildly unpredictable values; while the Modified NRW method delivers a lower value from the average (within 0.7% of the other methods). If it is initially assumed that the dielectric constant is non-dispersive across X-band, it is possible to compare extraction strategies (given their resulting standard deviations) for the five spot frequency values given in TABLE 6.

TABLE 7 shows the resulting averages for the spot frequency values and their standard deviations. It can be seen that, with both Samples #1 and #2, the Graphical and Renormalization approaches agree with one another and exhibit a very low standard deviation across X-band; effectively extracting non-dispersive values for dielectric constant of 2.329 and 2.309 for Sample #1 and Sample # 2, respectively, with discrepancies being attributed to arbitrary defects in the two 3-D printed samples and only having one frequency-swept measurement for each sample. The two NRW methods also agree with one another; with the Original method having a higher standard deviation and Modified method having a lower standard deviation, when both are

TABLE 6. Summary of dielectric properties for ABS extracted using various strategies.

Dielectric Property	Extraction Strategy		Frequencies [GHz] 8.20	9.00	10.00	11.1	12.40
Sample #1							
ε'_{reff} ($\tilde{\mu}_r = 1$)	Fabry-Pérot Resonance	M1	-	-	-	2.3250	-
		M3	-	-	-	2.3250	-
		M5	-	-	-	2.3284	-
	Graphical		2.3302	2.3210	2.3394	2.3250	2.3271
	Renormalization		2.3384	2.3240	2.3352	2.3254	2.3216
	Original NRW		2.2830	2.2831	2.2576	-	2.3450
$Re\{\tilde{\mu}_r\tilde{\varepsilon}_{reff}\}$	Modified NRW		2.3066	2.3085	2.3086	2.3103	2.3083
$\varepsilon''_{reff}/\varepsilon'_{reff} \times 10^4$ ($\tilde{\mu}_r = 1$)	Fabry-Pérot Resonance	M1	-	-	-	19.250	-
		M3	-	-	-	19.170	-
		M5	-	-	-	19.148	-
	Graphical		29.885	23.328	17.561	19.250	17.450
	Renormalization		29.693	22.220	19.455	19.023	16.910
	Original NRW		6.6063	19.259	56.025	-	-23.776
$Im\{\tilde{\mu}_r\tilde{\varepsilon}_{reff}\}/Re\{\tilde{\mu}_r\tilde{\varepsilon}_{reff}\} \times 10^4$	Modified NRW		27.796	24.510	25.464	23.888	22.393
Sample #2							
ε'_{reff} ($\tilde{\mu}_r = 1$)	Fabry-Pérot Resonance	M1	-	-	-	2.3045	-
		M3	-	-	-	2.3045	-
		M5	-	-	-	2.3080	-
	Graphical		2.3134	2.3089	2.3165	2.3043	2.3028
	Renormalization		2.3161	2.3077	2.3124	2.3045	2.3027
	Original NRW		2.2896	2.2988	2.2899	-	2.3044
$Re\{\tilde{\mu}_r\tilde{\varepsilon}_{reff}\}$	Modified NRW		2.3003	2.3046	2.3050	2.2999	2.3008
$\varepsilon''_{reff}/\varepsilon'_{reff} \times 10^4$ ($\tilde{\mu}_r = 1$)	Fabry-Pérot Resonance	M1	-	-	-	14.720	-
		M3	-	-	-	14.845	-
		M5	-	-	-	14.798	-
	Graphical		21.473	16.519	15.164	14.875	13.522
	Renormalization		21.311	14.945	14.455	14.718	13.417
	Original NRW		-12.914	9.9508	109.78	-	-242.8
$Im\{\tilde{\mu}_r\tilde{\varepsilon}_{reff}\}/Re\{\tilde{\mu}_r\tilde{\varepsilon}_{reff}\} \times 10^4$	Modified NRW		17.130	17.081	26.651	9.046	38.295

TABLE 7. X-band averages of dielectric constant extracted using various strategies.

	Dielectric Property	Extraction Strategy		Average	Standard Deviation
Sample #1	ε'_{reff} ($\tilde{\mu}_r = 1$)	Fabry-Pérot Resonance	M1	2.3250	-
			M3	2.3250	-
			M5	2.3284	-
		Graphical		2.3285	0.0069
		Renormalization		2.3289	0.0074
		Original NRW *		2.2922	0.0372
	$Re\{\tilde{\mu}_r\tilde{\varepsilon}_{reff}\}$	Modified NRW		2.3085	0.0013
Sample #2	ε'_{reff} ($\tilde{\mu}_r = 1$)	Fabry-Pérot Resonance	M1	2.3045	-
			M3	2.3045	-
			M5	2.3080	-
		Graphical		2.3092	0.0058
		Renormalization		2.3087	0.0055
		Original NRW *		2.2957	0.0072
	$Re\{\tilde{\mu}_r\tilde{\varepsilon}_{reff}\}$	Modified NRW		2.3021	0.0025
Pure ABS Sample **	Dielectric Constant	NRW		2.5750	0.0412
ABS-M30(LD) Sample **	Dielectric Constant	NRW		2.5575	0.0310
ABS-M30(SU) Sample **	Dielectric Constant	NRW		2.5450	0.0129

* excluding Fabry-Pérot resonance frequency value.
** using the quoted values taken from Deffenbaugh *et al.* [17].

compared to the Graphical and Renormalization approaches. However, the NRW methods give slightly lower values of dielectric constant (within 1.6% of the other methods). Nevertheless, this simple analysis confirms the initial assumption that the dielectric constant of ABS is non-dispersive across X-band. It can be seen from TABLE 6, with the Graphical and Renormalization approaches that, when ignoring the Fabry-Pérot resonance frequency, loss tangent for ABS decrease with increasing frequency across X-band. As a result, a non-dispersive analysis is not possible with loss tangent.

In contrast, from TABLE 5, while the average dielectric constants for all three ABS samples reported by Deffenbaugh *et al.* [17] are within 1.2% of each other, they are inflated by approximately 10% and have an order of magnitude increase in standard deviation, when compared to our results. Moreover, from TABLE 5, it can be seen that there is no consistent spectral trend in loss tangent.

Clearly, the dielectric properties for our FDM 3-D printed ABS do not corresponding to those for pure ABS or FDM 3-D printed ABS-M30 reported by Deffenbaugh *et al.* [17]. For example, with pure ABS between 8.2 GHz and 11 GHz, the reported extracted dielectric constant was 2.58±0.04 (±1.6% variation) with loss tangent fluctuating between 106 $\times 10^{-4}$ and 169 $\times 10^{-4}$ [19]; with very similar results for the FDM 3-D printed Stratasys ABS-M30 samples.

Since the results for ABS reported by Deffenbaugh *et al.* [17] does not include extracted data above 11 GHz, it can be inferred that they are likely to have adopted the Original NRW approach; with such a high recorded loss tangent, the effects of having f_{fp} ~13 GHz is likely to have restricted the upper frequency limit to *ca.* 11 GHz.

In summary, the Graphical and Renormalization approaches are in agreement with all the various Fabry-Pérot resonance modeling strategies, at the Fabry-Pérot resonance frequency; it does not assume a PEC-walled MPRWG or exhibit the mathematical instabilities or $\tilde{\mu}_r\tilde{\varepsilon}_{reff}$ ambiguity associated with the NRW methods. From all the various modeling strategies, there is general agreement in the dielectric properties extracted. Sample #1 has a frequency independent dielectric constant of 2.33 across X-band, while its loss tangent tends to decrease from 30×10^{-4} down to 17×10^{-4} as frequency increases across X-band. Sample #2 has a frequency independent dielectric constant of 2.31 across X-band, while its loss tangent tends to decrease from 21×10^{-4} down to 14×10^{-4} as frequency increases across X-band. These results are clearly less than those previously published in the open literature for pure ABS, shown in TABLE 5 [17].

IX. MEASUREMENT NOISE RESILIENCE ANALYSIS

With a modern space-domain Fourier-transform infrared (FTIR) spectrometer, the upper-bound *measurement* signal-to-noise power ratio (SNR or S/N) has a specific definition. With power transmission(reflection)-mode spectroscopy, without any sample under test, *signal* power $P_{reference}$ is represented by a 100% transmittance(reflectance) reference level (assuming no systematic errors within a calibrated system) and either the peak-to-peak or root-mean square (RMS) deviation from this reference level represents the generalized *noise* power P_{noise}, across the spectrum of interest [27]. With sub-millisecond integration times, FTIR systems have very low values of S/N [1]. Alternatively, the IRisF1 instrument (from IRsweep AG, Switzerland) is a quantum cascade laser frequency comb spectrometer that has $S/N|_{\mathrm{dB}} = 20$ dB with a 1 μs integration time (without any sample under test), which improves with integration time [28]. In contrast, modern frequency-domain VNAs can have a relatively high S/N, while terahertz time-domain spectroscopy (THz TDS) offers an extremely high S/N [1].

In practical metrology there may be numerous sources of measurement noise, having a variety of possible probability density function distributions. Within the limited scope of the analysis presented here, it is not feasible to investigate all possible sources of noise and their interactions within a modern commercial VNA. Nevertheless, it is assumed here that the overall noise from the various contributions exhibit an additive white Gaussian noise (AWGN) type of distribution. In addition, local oscillator phase noise can also be significant at higher frequencies; both assumed to be independent and uncorrelated. Investigating the impact of just AWGN can still reveal potential weaknesses with dielectric property extraction. For this reason, a simple AWGN-only analysis is undertaken.

First, the real and imaginary parts of noiseless S-parameters for S_{11} and S_{21} are mathematically emulated; this assumes a symmetrical and reciprocal scenario for a hypothetical non-magnetic dielectric sample under test. Based on the sample average extracted values from TABLE 6, at 9 GHz, this sample has a dielectric constant $\varepsilon'_{reff} = 2.31$ and loss tangent $\varepsilon''_{reff}/\varepsilon'_{reff} = 20\times10^{-4}$, as fixed target values for subsequent $\tilde{n}_{Target}$ extraction (with $n_{Target} = 1.51987$ and $\kappa_{Target} = 1.52\times10^{-3}$ at 9 GHz). This sample is then inserted into our simulated thru section of waveguide, modeled at 9 GHz using the *variational* method. These four noiseless S-parameter values effectively represent the simulation of four independent noiseless *'signal voltage measurements'* $v_{noiseless}$ to which independent and uncorrelated random noise voltages will be added (having AWGN distributions); effectively representing the emulation of 40 *'RMS noise voltage measurements'* v_{AWGN}. Within this limited study, only 10 noisy *'S-parameter measurements'* for both S_{11} and S_{21} were emulated at 9 GHz, represented by 40 noisy *'signal voltage measurements'* $v_{noisy} = v_{noiseless} + v_{noise}$, where $v_{noise} \rightarrow v_{AWGN}$. The 9 GHz spot frequency was chosen as it represents a featureless part of X-band (i.e., well away from any band-edges or resonance frequencies).

At this point, it is necessary to define the upper-bound *measurement* signal-to-noise power ratio in terms of effective *'RMS noise voltage measurements'* $v_{noise}|_{RMS}$. Here, the RMS FTIR spectrometer definition for the upper-bound *measurement* S/N is adopted, because it is independent of any

arbitrary S-parameter measurements:

$$S/N|_{\mathrm{dB}} = 10\log_{10}\{S/N\}$$

with

$$S/N = \frac{P_{reference}}{P_{noise}} = \frac{v_{noiseless}|^2_{RMS}}{v_{noise}|^2_{RMS}} \rightarrow S/N_{AWGN} = \frac{1}{v_{AWGN}|^2_{RMS}} \quad (93)$$

With (93), the specific level of $S/N|_{\mathrm{dB}}$, sets the upper RMS limit for $v_{noise} \rightarrow v_{AWGN}$. In practice, (93) is implemented with the built-in MATLAB function '*awgn*' [21] to produce 40 random sample values of v_{AWGN} within this RMS limit,

$$v_{AWGN} = awgn(v_{noiseless}, S/N_{AWGN}|_{\mathrm{dB}}) \quad (94)$$

It should be noted that while the real and imaginary parts of both S_{11} and S_{21} are assigned the same level of $S/N|_{\mathrm{dB}}$, using (94), this same level also independently applies exactly to both $|S_{11}|$ and $|S_{21}|$. Within our limited study, a broad range of $S/N|_{\mathrm{dB}}$ levels are investigated for extracting $\tilde{n}$, from 10 dB (poor sensitivity instruments) to 100 dB (high sensitivity instruments), in steps of 10 dB. In addition, noiseless values $\tilde{n}_{noiseless}$ are extracted as a benchmark for the various methodologies used within this paper.

The results using the various extraction strategies are show in FIGURE 18. With all methodologies, there is a greater spread on refractive index, when compared to the extinction coefficient, but in terms of percentage change the reverse is true. For all levels of $S/N|_{\mathrm{dB}}$, it can be seen that the scatter of extracted values for $\tilde{n}$ is less confined with the Original NRW method, when compared to the Modified NRW method. However, with the Original method the extracted values for $\tilde{n}$ cluster at a noiseless point $\tilde{n}_{noiseless}$ that is closer to the target value $\tilde{n}_{Target}$. This highlights a fundamental weakness with both NRW methodologies, in that $\tilde{n}_{noiseless} \neq \tilde{n}_{Target}$, since the ohmic losses associated with the conducting metal walls of the MPRWG are not considered. In contrast, with both Graphical and Renormalization methods, $\tilde{n}_{noiseless} = \tilde{n}_{Target}$.

The data spread in FIGURE 18 has been summarized in TABLE 8 with the use of a worst-case normalized *measurement* peak error vector magnitude $EVM\% = (EVM_{PEAK}/|\tilde{n}_{Target}|) \times 100\%$, where EVM_{PEAK} is the minimum radius for the circle that encompasses all 10 extracted $\tilde{n}$ points (from the 10 emulated noisy '*S-parameter measurements*' for S_{11} and S_{21}) with its center at $\tilde{n}_{Target}$. It is expected that EVM_{PEAK} dramatically increases as S/N degrades; this is seen in TABLE 8.

Alternatively, EVM_{RMS} can be defined as the RMS radius for the circles that correspond to the 10 extracted $\tilde{n}$ points with their center at $\tilde{n}_{Target}$. Within a linear system, given $\tilde{n}_{Target}$ and EVM_{RMS}, the corresponding S/N_{AWGN} can be estimated using an equation of the form [29],

$$\frac{EVM_{RMS}}{|\tilde{n}_{Target}|} \approx \begin{cases} \sqrt{\dfrac{1}{S/N_{AWGN}} + \sigma^2_{error}} \\ (S/N_{AWGN})^{-1/2} \text{ for } S/N_{AWGN}|_{\mathrm{dB}} \gtrsim 20 \text{ dB} \end{cases} \quad (95)$$

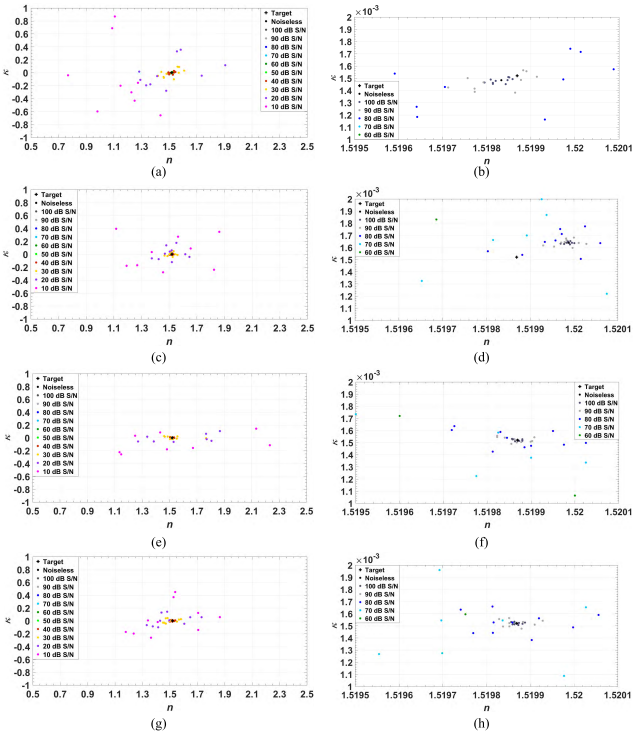

FIGURE 18. Noise sensitivity for a hypothetical dielectric sample having a fixed dielectric constant $\varepsilon'_{reff} = 2.31$ and loss tangent $\varepsilon''_{reff}/\varepsilon'_{reff} = 20 \times 10^{-4}$ (with $n_{Target} = 1.51987$ and $\kappa_{Target} = 1.52 \times 10^{-3}$ at 9 GHz) inserted into our simulated thru section of waveguide modeled at 9 GHz using the *variational* method: (a) zoomed-out Original NRW; (b) zoomed-in Original NRW; (c) zoomed-out Modified NRW; (d) zoomed-in Modified NRW from; (e) zoomed-out Graphical method; (f) zoomed-in Graphical method; (g) zoomed-out Renormalization method; and (h) zoomed-in Renormalization method.

TABLE 8. Worst-case normalized *measurement* peak error vector magnitudes from FIGURE 18 for different methodologies.

$S/N\|_{dB}$	*Measurement Peak EVM%*			
	Original NRW	Modified NRW	Graphical *	Renormalization
10	67.4308	67.3107	47.4651	71.2671
20	26.5339	11.7441	23.8831	14.4112
30	7.2725	3.7859	16.2645	4.9536
40	2.6203	1.2554	1.2817	1.5948
50	0.8692	0.3974	0.3755	0.4360
60	0.2811	0.1196	0.1181	0.1373
70	0.0915	0.0392	0.0417	0.0415
80	0.0312	0.0196	0.0122	0.0131
90	0.0121	0.0137	0.0039	0.0042
100	0.0061	0.0119	0.0011	0.0013
Noiseless	0.0033	0.0111	$55\text{x}10^{-6}$	$4\text{x}10^{-6}$

* using the maximum obtainable zoomed-in level to observe the graphs

where, σ_{error} is an RMS error in the extraction process (effectively representing additional uncorrelated noise). EVM_{RMS} is plotted in FIGURE 19 for different methodologies. It can be seen that all approaches generally follow the approximation given in (95). As S/N_{AWGN} increases, with both NRW approaches, EVM_{RMS} approaches their residual value $|\tilde{n}_{noiseless} - \tilde{n}_{Target}|$.

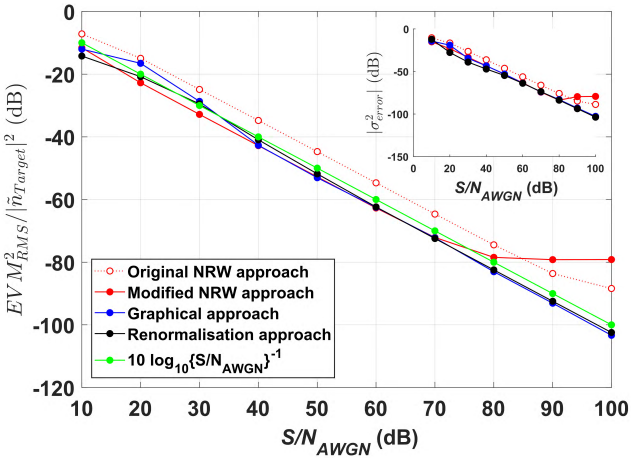

FIGURE 19. Normalized *measurement* RMS error vector magnitudes from FIGURE 18 for different methodologies.

In summary, errors in the extracted value of $\tilde{n}$ are negligibly small with the Graphical and Renormalization methods, while both NRW methodologies have significant errors that are inherent – due to the PEC-walled MPRWG assumption. As $S/N|_{\mathrm{dB}}$ degrades, both Graphical and Renormalization methods maintain their resilience as long as the minimum grid resolution can increase. Further improvements with the Renormalization method can be made by having a more aggressive port reference impedance optimization strategy.

Appendix C gives an analysis of the *measurement* $S/N|_{\mathrm{dB}}$ for the calibrated VNA system used to generate our S-parameters. A *measurement* $S/N|_{\mathrm{dB}}$ of 88.5 dB can be inferred, when based on the RMS approach. Therefore, it can be seen from TABLE 8 that in this particular example, the Graphical method has the lowest *measurement EVM%*.

X. DISCUSSION

To predict how effective an FDM 3-D printed ABS substrate could be at X-band, arithmetic average values (indicated by a bar accent) of the dielectric properties for Samples #1 and #2 were taken from TABLE 1, at the Fabry-Pérot resonance frequency of 11.1 GHz. Simple distributed- and lumped-element component exemplars can now be designed for hybrid microwave integrated circuit applications. Here, the unloaded Q-factor represents a crude figure-of-merit for both a microstrip transmission line and shunt capacitor. From TABLE 1, extracted using Fabry-Pérot resonance modeling, the predicted sample average effective conductivity $\overline{\sigma_d}$ = 2.4296 mS/m at 11.1 GHz, with a corresponding resistivity $\rho_d = 1/\overline{\sigma_d} = 41.16\ \mathrm{k\Omega \cdot cm}$. This confirms that our FDM 3-D printed ABS could be used as a high resistivity dielectric substrate for microwave applications, as well as providing a compatible high-performance RF conformal packaging solution (with additional processing required to provide a hermetic enclosure).

The Microwave Office® calculator *TX-LIN 2003* was first used to model a 50 Ω microstrip transmission line at 11.1 GHz, using sample average dielectric constant and loss tangent values of $\overline{\varepsilon'_{reff}} = 2.31475$ and $\overline{tan\delta_e} = 16.985 \times 10^{-4}$. With a substrate thickness $h = 500\ \mu$m, a 50 Ω microstrip line requires a track width $W_{TX} \cong 1.45$ mm; the wavelength $\lambda \cong 19.2$ mm and the specific attenuation is only 4.25 dB/m or ∼0.08 dB/λ at 11.1 GHz with 2 μm thick copper (one skin depth is 0.326 μm at 11.1 GHz). With $\alpha\lambda \cong 9.39$ mNp/λ, from (42), for an arbitrary length of uniform microstrip, the unloaded Q-factor $Q_U = \pi/\alpha\lambda \cong 335$ at 11.1 GHz. This compares favorably with M1 modeled dielectric-filled MPRWG Fabry-Pérot resonators, having $Q_U(f_{fp})$ of ∼490 and ∼620, with Samples #1 and #2, respectively.

A thin-film capacitor, having equal length $L_{CAP} = 3.7$ mm and width $W_{CAP} = 3.7$ mm dimensions, gives an area-to-separation distance ratio of $(A_{CAP}/h) = 0.0273$. Therefore, with a first-order model, the lumped-element parallel-plate capacitance $C_{pp} = \varepsilon_0\overline{\varepsilon'_{reff}}\,(A_{CAP}/h) = 0.561$ pF (ignoring ∼25% extra fringe capacitances) and shunt resistance $R_{pp} = \rho_d(h/A_{CAP}) = 15.033$ kΩ (ignoring ∼20% reduction due to the extra fringe capacitances); giving a very respectable PEC component unloaded Q-factor $Q_U = \omega C_{pp}R_{pp} \equiv Q_{0e} = 1/\overline{tan\delta_e} \cong 588$ at 11.1 GHz. Here, the effects of fringe capacitance were confirmed using the closed-form thin-film capacitor model in Microwave Office®.

Characterization of numerous non-ABS FDM 3-D printed dielectrics have been reported (in addition to those from Deffenbaugh *et al.* in 2013 [17]). For example, as with our work, a MakerBot Replicator 2X desktop printer having a 100% infill setting was recently used to characterize high impact polystyrene (HIPS); the reported dielectric constant was 2.452 and loss tangent was 5.73×10^{-4} [30]. Unfortunately, no methodology for extracting the dielectric properties was given. However, it was stated that S-parameter measurements were taken using a vector network analyzer (Agilent PNA-L N5230A) between 9 and 10 GHz for a 50 mm long dielectric-filled MPRWG within the EIA waveguide standard WR-112 band (7.05 to 10.00 GHz) and non-commercial 3-D software (OpenSCAD) was used. With a quoted sample size of $28.5 \times 12.6 \times 50\ \mathrm{mm}^3$, the theoretical Fabry-Pérot resonance frequency for a lossless scenario is calculated, using (27), to be $f_{fp} = 3.866$ GHz, (i.e., well below the recommended operational frequency range, with $f_c = 3.359$ GHz and $f_{c10} = 5.260$. GHz).

A recent development has been the FDM 3-D printing of polystyrene and cyclic olefin copolymer (TOPAS) rectangular dielectric waveguides at 120 GHz [31], using the Ultimaker3 (having a maximum layer resolution of 20 μm and nozzle size of 400 μm). Using a quasi-optical millimeter-wave system and curve fitting to measured data, the refractive index and absorption coefficients were reported. The respective dielectric constants and loss tangents at 120 GHz are 2.478 and 0.188×10^{-4} for polystyrene and 2.161 and 1.111×10^{-4} for TOPAS. This suggests that these materials offer major opportunities for FDM 3-D printed

TABLE 9. Extracted (sub-)terahertz dielectric properties for all photopolymer ABS samples reported by Duangrit *et al.* [34].

Dielectric Property	Spot Frequencies [GHz]		
	200	800	1400
Polyjet printed 1.05 mm thick Stratasys ABS Flex			
Dielectric Constant	2.934	2.821	2.762
Loss Tangent $\times 10^4$	190	590	760
DLP printed 2.84 mm thick EnvisionTEC ABS Tough			
Dielectric Constant	2.893	2.800	2.735
Loss Tangent $\times 10^4$	120	510	720
DLP printed 2.97 mm thick EnvisionTEC ABS Flex Black			
Dielectric Constant	2.807	2.722	2.656
Loss Tangent $\times 10^4$	210	570	780

high-resistivity substrates and dielectric-based components for future microwave, millimeter-wave and terahertz applications.

Modern THz TDS techniques have serious limitations when used to accurately extract dielectric properties [1]. This was also the conclusion from a 2016 inter-comparison material characterization study using THz TDS, between international laboratories [32]. Indeed, when compared to frequency-domain microwave VNA measurements using internationally traceable calibration standards, accurate material characterization with terahertz VNA measurements is still challenging [33]. A 2017 material characterization inter-comparison study between THz TDS, FTIR spectroscopy and THz VNA measurements indicated a lack of equivalence in extracted complex refractive indices, between all techniques, at frequencies as low as 300 GHz (and below), with even negative mean values of extinction coefficients reported with THz TDS for fused quartz and Pyrex at 400 GHz [33].

Nevertheless, an attempt to accurately characterize 3-D printed photopolymers using THz TDS has been recently reported [34]. For example, results from [34] for photopolymer ABS samples are given in TABLE 9, when 3-D printed using either polymer-jetting (Polyjet) or digital-light processing (DLP); both being more advanced additive manufacturing techniques when compared to FDM 3-D printing of ABS thermoplastic filaments [4].

The dielectric properties between photopolymer ABS samples generally agree with one another. It is interesting to note that the extracted dielectric constants are significantly higher in value than those reported here and in [17] for X-band (although close to the quoted data sheet value of 2.8 for all ABS samples in [17]) and decrease with increasing frequency (i.e., exhibiting frequency dispersion over the large 150% fraction bandwidth of the measurements). Moreover, the loss tangents are an order of magnitude greater than those reported here for X-band, while also increasing with frequency. However, caution should be applied when comparing results, due to fundamental differences: (i) between the chemically different photopolymer ABS and our ABS thermoplastics; (ii) in printing technologies; (iii) in the measurement frequencies, being two orders of magnitude higher than those at X-band; and (iv) in methodologies for extracting the dielectric properties. Nevertheless, even with such high loss tangents, a similar photopolymer (HTM140-V2, with loss tangent of 230×10^{-4} at 200 GHz) demonstrated an asymptotically single-mode Bragg fiber having a measured specific attenuation of only 3 dB/m at 260 GHz [34].

XI. CONCLUSION

Both the manual Graphical and automated Renormalization approaches are in agreement with all the Fabry-Pérot resonance modeling strategies, at the Fabry-Pérot resonance frequency; automation being the method of choice when time is an important consideration. It has been shown that these two new spectroscopic approaches avoid the three fundamental limitations to accuracy found with the NRW methods: (i) they do not assume PEC-walled MPRWGs, which would otherwise result in extracted dielectric properties being different to the true values (the importance of this point increases as the sample-to-MPRWG loss ratio decreases), unless numerical methods are used; (ii) dielectric property extraction exhibits less sensitivity to measurement noise, when compared to the Original NRW method (about the same with the Modified NRW method), as presented in a featureless part of the frequency range of interest; (iii) the reduction in the useful waveguide bandwidth (avoiding the Fabry-Pérot resonance) with the Original NRW method and $\tilde{\mu}_r\tilde{\varepsilon}_{reff}$ restriction to non-magnetic materials with the Modified NRW method are avoided. Moreover, even greater accuracy than shown here can be obtained with both new spectroscopic approaches, by increasing their minimum grid resolutions and applying further constraints.

From all the various modeling strategies there is general agreement in the dielectric properties extracted. Having relatively more noisy measurements, Sample #1 has a frequency independent dielectric constant of 2.33 across X-band, while its loss tangent tends to decrease from 30×10^{-4} down to 17×10^{-4} as frequency increases across X-band. Having less noisy measurements, Sample #2 has a frequency independent dielectric constant of 2.31 across X-band, while its loss tangent tends to decrease from 21 $\times10^{-4}$ down to 14 $\times10^{-4}$ as frequency increases across X-band. These results are significantly those previously published in the open literature for pure ABS and FDM 3-D printed Stratasys ABS-M30 samples [17]; offering the possibility of realizing FDM 3-D printed high-resistivity substrates and dielectric-based components (e.g., solid and flat graded-index quasi-optical dielectric lenses [35]).

Signal-to-noise ratios for VNAs depend on numerous operational settings and configurations. However, by adopting techniques from FTIR spectrometers, a methodology has been demonstrated for evaluating the upper-bound signal-to-noise ratio using the simple measurement noise resilience analysis presented in this paper. Finally, the non-homogeneity resulting from voids within FDM 3-D printed samples have

been found to excite open-box mode resonances. This phenomenon has been investigated for the first time, analytically and with various modeling strategies.

In summary, this paper has introduced several new techniques, based on limited swept frequency measurements, for two dielectric samples. It is believed that this collection of interrelated studies can be developed further, while also being applied to other material systems. Areas for further development include: incorporating a detailed uncertainty analysis for the samples under test; developing quantitative non-analytical models for open-box mode resonances; further improvements to NRW methods; and, investigating the influence of non-AWGN on measurement S/N.

APPENDIX A

Consider the waveguide structure shown in FIGURE 3, where a TE wave is incident on a dielectric-filled section of MPRWG. Under steady-state sinusoidal excitation, there will be forward and backward traveling waves, with A representing the complex amplitude coefficients for the forward traveling waves and B representing the backward traveling waves. There are no reflected waves within Section ③ of the waveguide structure. It is assumed that Sections ①, ③ have the same material parameters. For the $\mathrm{TE_{mn}}$ mode, the electric (E-)field and magnetic (H-)field components within the three waveguide sections are [36],

$$E_{y①} = \frac{\omega\tilde{\mu}_① \gamma_{cm0}}{\gamma_{cmn}^2}\left(A_{\mathrm{mn}①}e^{-\gamma_{mn①}z} + B_{\mathrm{mn}①}e^{\gamma_{mn①}z}\right) \times \sin(k_{cm0}x)\cos(k_{c0n}y) \quad (96)$$

$$H_{x①} = -j\frac{\gamma_{mn①}\gamma_{cm0}}{\gamma_{cmn}^2}\left(A_{\mathrm{mn}①}e^{-\gamma_{mn①}z} - B_{\mathrm{mn}①}e^{\gamma_{mn①}z}\right) \times \sin(k_{cm0}x)\cos(k_{c0n}y) \quad (97)$$

$$H_{z①} = \left(A_{\mathrm{mn}①}e^{-\gamma_{mn①}z} - B_{\mathrm{mn}①}e^{\gamma_{mn①}z}\right) \times \cos(k_{cm0}x)\cos(k_{c0n}y) \quad (98)$$

$$E_{y②} = \frac{\omega\tilde{\mu}_② \gamma_{cm0}}{\gamma_{cmn}^2}\left(A_{mn②}e^{-\gamma_{mn②}z} + B_{\mathrm{mn}②}e^{\gamma_{mn②}z}\right) \times \sin(k_{cm0}x)\cos(k_{c0n}y) \quad (99)$$

$$H_{x②} = -j\frac{\gamma_{mn②}\gamma_{cm0}}{\gamma_{cmn}^2}\left(A_{mn②}e^{-\gamma_{mn②}z} - B_{\mathrm{mn}②}e^{\gamma_{mn②}z}\right) \times \sin(k_{cm0}x)\cos(k_{c0n}y) \quad (100)$$

$$H_{z②} = \left(A_{mn②}e^{-\gamma_{mn②}z} - B_{\mathrm{mn}②}e^{\gamma_{mn②}z}\right) \times \cos(k_{cm0}x)\cos(k_{c0n}y) \quad (101)$$

$$E_{y③} = \frac{\omega\tilde{\mu}_① \gamma_{cm0}}{\gamma_{cmn}^2}A_{mn③}e^{-\gamma_{mn①}(z-l)} \times \sin(k_{cm0}x)\cos(k_{c0n}y) \quad (102)$$

$$H_{x③} = -j\frac{\gamma_{mn①}\gamma_{cm0}}{\gamma_{cmn}^2}A_{mn③}e^{-\gamma_{mn①}(z-l)} \times \sin(k_{cm0}x)\cos(k_{c0n}y) \quad (103)$$

$$H_{z③} = A_{mn③}e^{-\gamma_{mn①}(z-l)}\cos(k_{cm0}x)\cos(k_{c0n}y) \quad (104)$$

where,

$$\gamma_{cmn} = jk_{cmn} = j\sqrt{\left(\frac{m\pi}{a}\right)^2 + \left(\frac{n\pi}{b}\right)^2} \quad (105)$$

and,

$$k_{cm0} = \frac{m\pi}{a} \quad \text{and} \quad k_{c0n} = \frac{n\pi}{b} \quad (106)$$

Here, $\gamma_{mn①}$ and $\gamma_{mn②}$ are the generalized propagation constants for the $\mathrm{TE_{mn}}$ modes within Sections ①, ③, and Section ②, respectively. With respect to FIGURE 3, $\gamma_{mn①} \rightarrow \gamma_{10}^{air}$ and $\gamma_{mn②} \rightarrow \gamma_{10}$ are the propagation constants for the $\mathrm{TE_{10}}$ mode within the air-filled (Sections ① ③,) and dielectric-filled (Section ②) waveguide sections, respectively; all calculated using (1) for finite wall conductivity waveguides. The reference plane for coefficients $A_{mn③}$ is $z = l$ as indicated by the $z - l$ shift in the term $A_{mn③}e^{-\gamma_{mn①}(z-l)}$. The reference plane for all other coefficients is $z = 0$.

By applying boundary conditions: $E_{y①}(z=0) = E_{y②}(z=0)$, $E_{y②}(z=l) = E_{y③}(z=l)$, $H_{x①}(z=0) = H_{x②}(z=0)$, $H_{x②}(z=l) = H_{x③}(z=l)$, and after some algebraic manipulations, the following is obtained,

$$\begin{bmatrix} \tilde{\mu}_① & \tilde{\mu}_① & -\tilde{\mu}_② & -\tilde{\mu}_② & 0 \\ \gamma_{mn①} & -\gamma_{mn①} & -\gamma_{mn②} & \gamma_{mn②} & 0 \\ 0 & 0 & \tilde{\mu}_② e^{-\gamma_{mn②}l} & \tilde{\mu}_② e^{\gamma_{mn②}l} & -\tilde{\mu}_① \\ 0 & 0 & \gamma_{mn②}e^{-\gamma_{mn②}l} & -\gamma_{mn②}e^{\gamma_{mn②}l} & -\gamma_{mn①} \end{bmatrix} \cdot \begin{bmatrix} A_{mn①} \\ B_{mn①} \\ A_{mn②} \\ B_{mn②} \\ A_{mn③} \end{bmatrix} = \begin{bmatrix} 0 \\ 0 \\ 0 \\ 0 \end{bmatrix} \quad (107)$$

For convenience, the waveguide structure in FIGURE 3 is excited by setting $A_{mn①}$ to unity and the rest of the amplitude coefficients can then be obtained from (107) as,

$$B_{mn①} = \frac{\left(1 - e^{-2\gamma_{mn②}l}\right)(1-\zeta)(1+\zeta)}{(1+\zeta)^2 - e^{-2\gamma_{mn②}l}(1-\zeta)^2} \quad (108)$$

$$A_{mn②} = \frac{-2\varsigma(1+\zeta)}{(1+\zeta)^2 - e^{-2\gamma_{mn②}l}(1-\zeta)^2} \quad (109)$$

$$B_{mn②} = \frac{-2\varsigma e^{-2\gamma_{mn②}l}(1-\zeta)}{(1+\zeta)^2 - e^{-2\gamma_{mn②}l}(1-\zeta)^2} \quad (110)$$

$$A_{mn③} = \frac{4\zeta e^{-\gamma_{mn②}l}}{(1+\zeta)^2 - e^{-2\gamma_{mn②}l}(1-\zeta)^2} \quad (111)$$

with generalized coefficients,

$$\zeta = \begin{cases} \dfrac{\gamma_{mn①}}{\gamma_{mn②}}\varsigma & \mathrm{TM_{mn}\ modes} \\ \dfrac{\gamma_{mn②}}{\gamma_{mn①}}\varsigma & \mathrm{TE_{mn}\ modes} \end{cases} \quad (112)$$

and,

$$\varsigma = \begin{cases} \dfrac{\tilde{\varepsilon}_②}{\tilde{\varepsilon}_①} & \mathrm{TM_{mn}\ modes} \\ \dfrac{\tilde{\mu}_①}{\tilde{\mu}_②} & \mathrm{TE_{mn}\ modes} \end{cases} \quad (113)$$

where,

$$S_{11} \equiv \left.\frac{B_{mn①}}{A_{mn①}}\right|_{B_{\mathrm{mn}③}=0} \rightarrow B_{mn①} \quad \text{with} \quad A_{mn①} = 1 \quad (114)$$

and,

$$S_{21} \equiv \left.\frac{A_{mn③}}{A_{mn①}}\right|_{B_{mn③}=0} \rightarrow A_{mn③} \quad \text{with} \quad A_{mn①} = 1 \tag{115}$$

Therefore, with no waveguide wall or dielectric losses, at the Fabry-Pérot resonance frequency, there is a return loss zero with $B_{mn①} = 0$ and $A_{mn③} = 1$.

With a PEC-walled waveguide, the propagation constant for an unbound dielectric is given from (2) as,

$$\gamma_{ud}^2 = \gamma_{mn}^2 + \gamma_{cmn}^2 = -\omega^2\tilde{\mu}\tilde{\varepsilon} \tag{116}$$

With the scenario depicted in FIGURE 3, $\tilde{\mu}_{①,③} = \mu_0\tilde{\mu}_{r①,③} \rightarrow \mu_0$, $\tilde{\mu}_{②} = \mu_0\tilde{\mu}_{r②} \rightarrow \mu_0\mu_r'$, $\tilde{\varepsilon}_{①,③} = \varepsilon_0\tilde{\varepsilon}_{reff①,③} \rightarrow \varepsilon_0$ and $\tilde{\varepsilon}_{②} = \varepsilon_0\tilde{\varepsilon}_{reff②} \rightarrow \varepsilon_0\tilde{\varepsilon}_{reff}$. Therefore, the respective waveguide propagation constants for Sections ① ,③ and Section ② are,

$$\gamma_{mn①,③} = \sqrt{k_{cmn}^2 - \omega^2\tilde{\mu}_{①,③}\tilde{\varepsilon}_{①,③}} \rightarrow \sqrt{k_{cmn}^2 - \omega^2\mu_0\varepsilon_0} \tag{117}$$

and,

$$\gamma_{mn②} = \sqrt{k_{cmn}^2 - \omega^2\tilde{\mu}_{②}\tilde{\varepsilon}_{②}} \rightarrow \sqrt{k_{cmn}^2 - \omega^2\mu_0\mu_r'\varepsilon_0\tilde{\varepsilon}_{reff}} \tag{118}$$

Now, the total energy stored inside the dielectric sample under test W_T can be computed from,

$$W_T = W_M + W_E \tag{119}$$

where, W_M and W_E are the time-averaged magnetic and electric energies, respectively, given by the volume integrals (where the total volume of the dielectric sample under test $V = a \times b \times l$) [36],

$$W_M = \frac{\mu_0\mu_r'}{4}\langle\int_v |H_{x②}|^2 + |H_{Z②}|^2\, dv\rangle \tag{120}$$

$$W_E = \frac{\varepsilon_0\varepsilon_{reff}'}{4}\langle\int_v |E_{y②}|^2\, dv\rangle \tag{121}$$

At the Fabry-Pérot resonance frequency, the loaded Q-factor for the TE_{10} mode can be calculated by considering the loss contributions to the total dissipated power $P_T = P_c + P_d + P_e$, where P_c is due to the waveguide's conducting wall losses, P_d is due to the dielectric losses and P_e is due to the external impedance loading at both waveguide test ports. The corresponding constituent Q-factor components given in (41) are then,

$$Q_c = \omega_{fp}\frac{W_T}{P_c} \tag{122}$$

$$Q_d = \omega_{fp}\frac{W_T}{P_d} \tag{123}$$

$$Q_e = \omega_{fp}\frac{W_T}{P_e} \tag{124}$$

where, the corresponding time-average power dissipation contributions can be computed from [36],

$$P_c = R_s\langle\int_{x=0} |H_{x②}|^2\, ds\rangle + R_s\langle\int_{y=0} \left(|H_{x②}|^2 + \left|H_{z②}\right|^2\right) ds\rangle \tag{125}$$

$$P_d = \frac{\sigma_d}{2}\langle\int_v |E_{y②}|^2\, dv\rangle \tag{126}$$

$$P_e = \frac{1}{2}Re\left\{\langle\int_{z=0} \left(E_{y①} \times H_{x①}^*\right) ds\rangle + \langle\int_{z=l} \left(E_{y③} \times H_{x③}^*\right) ds\rangle\right\} \tag{127}$$

The field integrals given in (120)-(121) and (125)-(127) (contained within the angle brackets $\langle\ \rangle$) are either calculated analytically, using (107)-(113) with the resulting fields defined by (96)-(104), or computed within *COMSOL Multiphysics*®; the results are shown in the bottom half of TABLE 3.

APPENDIX B

A. QUALITATIVE EXCITATION OF OPEN-BOX MODE RESONANCES WITH FREQUENCY-DOMAIN SOLVER

Open-box modes can be excited by non-homogeneities. With our FDM 3-D printed samples, open-box modes reveal themselves as notches in frequency-domain S-parameter measurements. Numerical modeling of a to-scale 3-D woodpile metamaterial structure is not possible, due to the extremely fine meshing required to model the very small spatial features seen in FIGURE 2. However, an artificial non-homogeneity can be introduced by using coarse meshing with a homogeneous structure. The sample was simulated using a mesh having only 84 tetrahedral elements, as shown in FIGURE 20(a). The corresponding frequency-domain simulated S-parameters in FIGURE 20(b) clearly show excitation of the expected open-box mode resonances at their predicted frequencies.

B. OPEN-BOX MODE RESONANCE FIELD PLOTS FROM EIGENMODE SOLVER

Numerical simulations using the eigenmode solver with fine meshing can be used to study the open-box mode resonances. Here, the two air-filled waveguide sections have been increased in length to $l_{air} = 11.5l$, allowing the evanescent fields of the open-box modes to sufficiently decay outside of the sample. Also, the extreme ends of the air-filled sections are terminated with *second-order scattering* boundary conditions [18], which help to absorb incident waves. FIGURES 21 to 23 show field plots of open-box mode resonances from the eigenmode solver for Sample #1.

It can be clearly seen in FIGURE 20(b) that the open-box mode resonances observed with coarse meshing are only slightly higher (with less than ~1% error) in frequency than those predicted with fine meshing, for the same dielectric constant and loss tangent values; making the former a useful technique with limited computational resources.

C. ANALYTICAL MODELING OF OPEN-BOX MODE RESONANCES

The TE_{mnp} open-box mode resonances observed with a dielectric-filled waveguide section can be modeled by

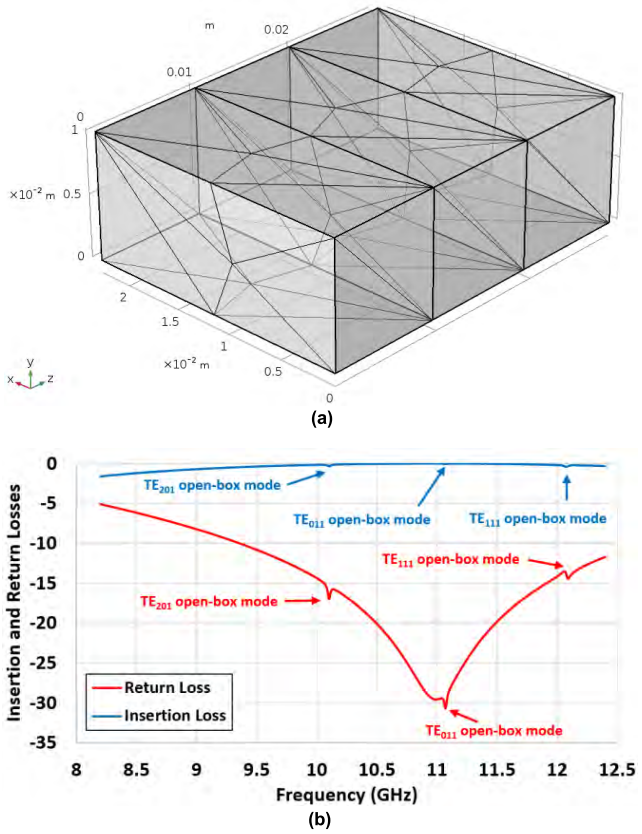

FIGURE 20. Numerical modeling of open-box mode excitation for Sample #1 with dielectric constant and loss tangent of 2.3284 and 19.148×10^{-4}, respectively, from M5 using coarse meshing: (a) 3-D coarse meshing of the complete structure illustrated in FIGURE 3, with $l_{air} = l$; and (b) resulting S-parameters showing open-box mode resonances at 10.17, 11.15 and 12.18 GHz.

extending the analysis given in APPENDIX A. The associated complex eigenfrequencies are defined by the poles of $B_{mn①}$ in (108), by setting its denominator to zero (i.e., to extract its natural modes, without any external steady-state sinusoidal excitation so that $A_{mn①} = 0$),

$$(1+\zeta)^2 - e^{-2\gamma_{mn②}l}(1-\zeta)^2 = 0 \tag{128}$$

An infinite number of solutions emerge from (128), which are either designated as even or odd modes depending on the corresponding symmetry of the electric fields. These even and odd modes can be obtained by solving the following equations for complex eigenfrequencies,

$$(1+\zeta) + e^{-\gamma_{mn②}l}(1-\zeta) = 0 \quad \text{Even modes} \tag{129}$$

$$(1+\zeta) - e^{-\gamma_{mn②}l}(1-\zeta) = 0 \quad \text{Odd modes} \tag{130}$$

After some algebraic manipulations, the following transcendental equations are obtained for TE modes,

$$\tilde{\mu}_① \gamma_{mn②} - \tilde{\mu}_② \gamma_{mn①} \coth\left(\frac{\gamma_{mn②}l}{2}\right) = 0 \quad \text{Even modes} \tag{131}$$

$$\tilde{\mu}_① \gamma_{mn②} - \tilde{\mu}_② \gamma_{mn①} \tanh\left(\frac{\gamma_{mn②}l}{2}\right) = 0 \quad \text{Odd modes} \tag{132}$$

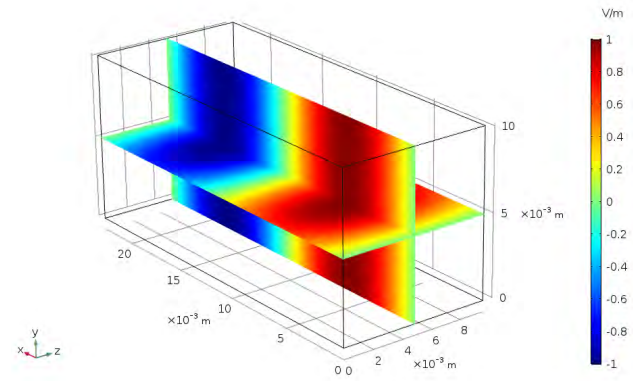

FIGURE 21. Numerically simulated E_y-field plot for TE_{201} open-box mode at $f_{201} = 10.074$ GHz for Sample #1 with dielectric constant and loss tangent of 2.3284 and 19.148×10^{-4}, respectively, from M5.

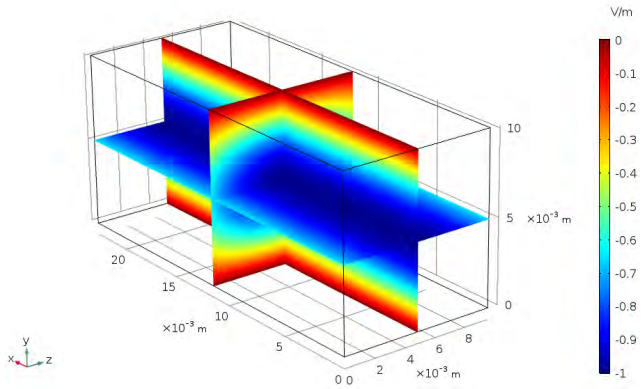

FIGURE 22. Numerically simulated E_x-field plot for TE_{011} open-box mode at $f_{011} = 11.144$ GHz for Sample #1 with dielectric constant and loss tangent of 2.3284 and 19.148×10^{-4}, respectively, from M5.

These generalized expressions can be simplified by setting $\tilde{\mu}_① = \tilde{\mu}_②/\mu_r' = \mu_0$ to obtain,

$$\mu_r' \gamma_{mn①} - \gamma_{mn②} \tanh\left(\frac{\gamma_{mn②}l}{2}\right) = 0 \quad \text{Even modes} \tag{133}$$

$$\gamma_{mn②} - \mu_r' \gamma_{mn①} \tanh\left(\frac{\gamma_{mn②}l}{2}\right) = 0 \quad \text{Odd modes} \tag{134}$$

The roots of (133) and (134) can be numerically solved to obtain the complex angular eigenfrequencies $\tilde{\omega}_{mnp} = \omega'_{mnp} + j\omega''_{mnp}$ for the even and odd TE_{mnp} open-box modes, respectively; the undamped (or driven) resonance frequencies, normally associated with frequency-domain simulations, is $f_{mnp} = |\tilde{\omega}_{mnp}|/2\pi$. Here, the multiple solutions from (133) and (134) correspond to different values of p. It is found, in our case, that the TE_{101}, TE_{201}, TE_{011} and TE_{111} modes all have even longitudinal symmetry about the center of the sample.

It should be noted that the dominant TE_{101} open-box mode, which is loosely related to the Fabry-Pérot resonance (in terms of field patterns) is predicted to exist at 5.6065 GHz and 5.6229 GHz for Samples #1 and #2, respectively. These are above our dielectric-filled waveguide cut-off frequencies

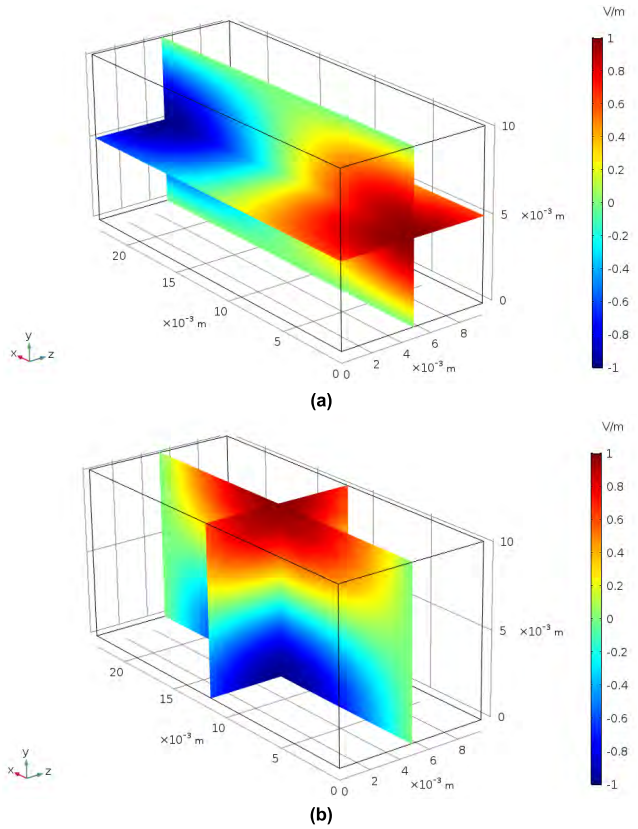

FIGURE 23. Numerically simulated field plots for TE_{111} open-box mode at $f_{111} = 12.046$ GHz for Sample #1 with dielectric constant and loss tangent of 2.3284 and 19.148×10^{-4}, respectively, from M5: (a) E_y-field; and (b) E_x-field.

f_c of 4.30 GHz and 4.32 GHz, respectively, but below the recommended operational frequency range of WR-90 waveguide. It has been confirmed that f_{101} is relatively low because the evanescent fields outside of the dielectric sample decay exponentially over a relatively long distance.

For completeness, a similar approach can be used to derive the following generalized equations for the TM_{mnp} open-box modes (with the lowest-order TM_{111} mode having an eigenfrequency of $f_{111} = 12.8765$ GHz, which is just above our frequency range of interest), with $\tilde{\varepsilon}_{①} = \tilde{\varepsilon}_{②}/\tilde{\varepsilon}_{reff} = \varepsilon_0$,

$$\tilde{\varepsilon}_{reff}\,\gamma_{mn①} - \gamma_{mn②}\tanh\left(\frac{\gamma_{mn②}l}{2}\right) = 0 \quad \text{Odd modes} \quad (135)$$

$$\gamma_{mn②} - \tilde{\varepsilon}_{reff}\,\gamma_{mn①}\tanh\left(\frac{\gamma_{mn②}l}{2}\right) = 0 \quad \text{Even modes} \quad (136)$$

D. QUALITATIVE EQUIVALENT CIRCUIT MODELING OF OPEN-BOX MODE RESONANCES

It is interesting to see if the open-box mode resonances can be modeled with the use of equivalent circuit models. Using Microwave Office®, it was found that it is possible to create a qualitative model for each mode with Sample #1, as seen in FIGURE 24.

The total length of the dielectric-filled MPRWG was partitioned into four sections, having lengths of $3.213 + 1.6 + 1.6 + 3.213 = 9.626$ mm. Between each section

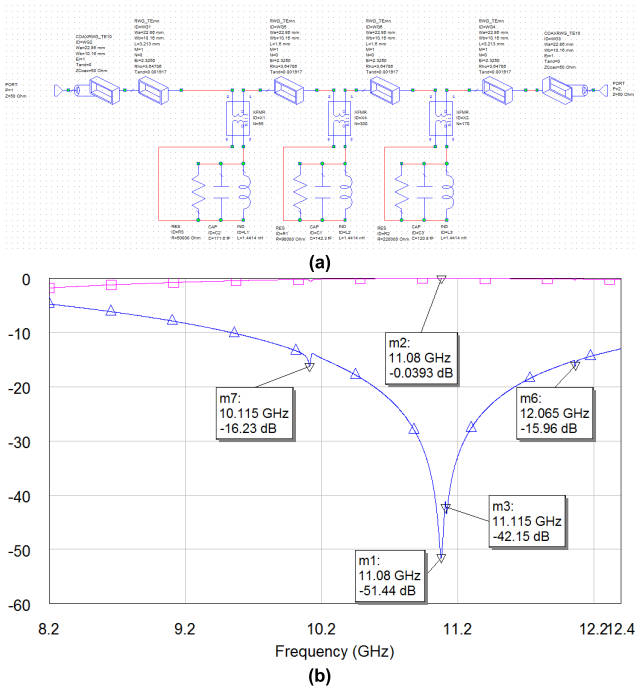

FIGURE 24. Qualitative equivalent circuit modeling of open-box mode resonances for Sample #1 in Microwave Office®: (a) circuit employing three lumped-element RLC resonators, each coupled with an ideal transformer; (b) simulated frequency-domain response.

a unique open-box mode model is inserted. Here, the primary winding of an ideal transformer is placed in series between adjacent MPRWG sections; with a specific turns ratio, a unique parallel RLC tuned circuit is connected across the secondary winding. For convenience, in order to minimize the number of variables, the inductor was kept constant for all the open-box mode models (having a value of 1.4414 nH), while the individual resonance frequencies were set by the capacitance and mode dampening was largely set by the resistance. By careful hand tuning, to avoid introducing mathematical instabilities in the simulated results, it was found that a reasonable facsimile of the frequency responses seen in FIGURE 20(b) can be recreated with: lowest $Q_u(10.120\text{ GHz})|_{TE201} = 546$, coupled most with 55:1 turns ratio; $Q_u(11.113\text{ GHz})|_{TE011} = 894$, coupled least with 300:1 turns ratio; and highest $Q_u(12.061\text{ GHz})|_{TE111} = 2,014$ coupled with 170:1 turns ratio. When compared to TABLE 4, the values of unloaded Q-factor are within an order of magnitude, but not accurate. This is because the ideal transformers and their levels of coupling are not taken into account. Moreover, the distribution of the transformed RLC tuned circuits can have a significant influence on individual unloaded Q-factors, with interactive couplings between RLC tuned circuits. As a result, the approach presented here highlights such issues.

APPENDIX C

It is interesting to estimate the upper-bound *measurement* $S/N|_{\text{dB}}$ for the calibrated VNA system (Agilent E8364C PNA Network Analyzer [37]) used to generate our

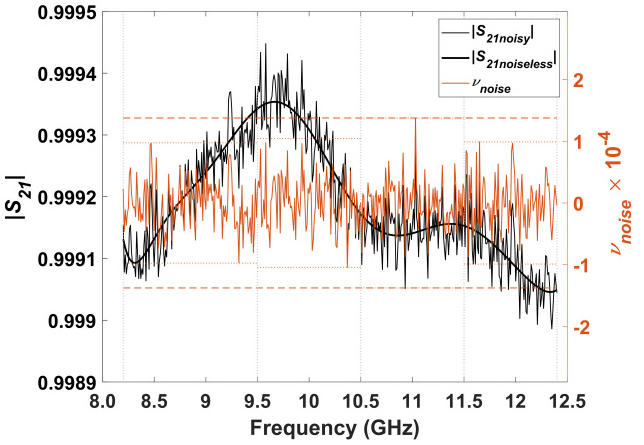

FIGURE 25. Measured $|S_{21}|$ for the air-filled 9.626 mm long thru line section of MPRWG, with its running average and extracted random noise components.

S-parameters. It is assumed here that the signal to noise power ratio is frequency independent across X-band. Noise represents a random deviation from the noiseless measurements, plotted against frequency, but considered as a sequence of sample points. First, the adopted RMS definition for a transmission mode FTIR spectrometer is used, with 421 spectral measurements from 8.2 to 12.4 GHz (in 0.01 GHz steps). The S_{21} and S_{12} for the air-filled 9.626 mm long thru line section of MPRWG were measured, with the results for $|S_{21}| = |S_{21noisy}| \rightarrow v_{noisy}$ shown by the thin black curve in FIGURE 25. The 10-point running average is estimated using the built-in MATLAB *'polyfit'* function [21], to give $|S_{21noiseless}| \rightarrow v_{noiseless} \neq 1$ illustrating the effects of systematic errors within the calibrated instrument, shown by the bold black curve in FIGURE 25. The running average is then subtracted from the measured response, to give the random noise spectral response v_{noise} centered around zero, shown in FIGURE 25. By taking the Fourier transform of v_{noise} extracted from measurements and comparing this with v_{AWGN} generated previously, it is found that they have almost identical probability density functions; confirming our initial assumption that AWGN dominates.

It is then possible to estimate the *measurement* $S/N|_{\text{dB}}$,

$$S/N|_{\text{dB}} = 10\log_{10}\left\{\frac{v_{noiseless}|_{RMS}}{v_{noise}|_{RMS}}\right\}^2 \tag{137}$$

Given $v_{noiseless}$ and v_{noise}, (137) is implemented using the inverse of (94) with the built-in MATLAB function '*snr*' [21],

$$S/N|_{\text{dB}} = snr\,(v_{noiseless}, v_{noise}) \tag{138}$$

The peak-to-peak representation of the signal-to-noise power ratio $S/N|_{\text{dB},p-p}$ can be defined as,

$$S/N|_{\text{dB},p-p} = 10\log_{10}\left\{\frac{1}{v_{noise}|_{p-p}}\right\}^2$$

TABLE 10. Upper-bound *Measurement* $S/N|_{\text{dB}}$ summary for the calibrated Agilent E8364C PNA Network Analyzer calibrated in waveguide at X-band.

Band [GHz]	*Measurement S/N* [dB]			
	RMS		Peak-to-Peak	
	S_{21}	S_{12}	S_{21}	S_{12}
8.2-12.4	88.2	88.7	71.2	72.9
8.2-9.5	88.3	89.2	74.2	75.2
9.5-10.5	87.9	87.8	73.6	74.3
10.5-11.5	89.0	89.3	71.2	75.4
11.5-12.4	87.7	88.4	74.1	72.9

with

$$v_{noise}|_{p-p} = 2\,|v_{noise}|_{MAX} \tag{139}$$

Given v_{noise}, (139) is implemented with the built-in MATLAB function '*max*' [21],

$$|v_{noise}|_{MAX} = max\,(abs(v_{noise})) \tag{140}$$

Using this simplified approach, it has been found that *measurement* $S/N|_{\text{dB}}$ is approximately 88.5 dB and 72.0 dB when based on RMS and peak-to-peak approaches, respectively, from our VNA measurements. A more detailed sub-band breakdown is shown in TABLE 10. It is seen in TABLE 10 that all four sub-bands have a *measurement* $S/N|_{\text{dB}}$ within a very narrow range, between 88 dB and 89 dB, with the RMS approach, which justifies our initial assumption that *measurement* $S/N|_{\text{dB}}$ is independent of frequency across X-band. The peak-to-peak approach exhibits a wider range, between 71 dB and 75 dB, due to the single point outliers that are observed in FIGURE 25.

It is interesting to note that for the Agilent E8364C PNA, the specification standard test port input noise floor is less than approximately -117.0 dBm (at X-band within an IF bandwidth of 10 Hz); increasing with IF bandwidth) [37]. At 10 GHz, the output signal power at the reference plane was measured to be -18.5 dBm, giving $S/N|_{\text{dB}} \gtrsim 98.5$ dB; decreasing with increasing IF bandwidth. Therefore, for a 100 Hz IF bandwidth, $S/N|_{\text{dB}} \gtrsim 88.5$ dB. This corresponds exactly to the independently extracted arithmetic average value from S_{21} and S_{12}, when based on our RMS approach across X-band, as shown in TABLE 10.

ACKNOWLEDGMENT

The authors would like to thank Dr. Mario D'Auria for printing the original dielectric samples under test and verifying the ABS filament source and 3-D printer used. The authors would also like to thank Dr. James Watts, at Flann Microwave Ltd. (U.K.), for providing material information for the quarter-wave thru line waveguide, and James Skinner at the U.K.'s National Physical Laboratory, for

measuring the output signal power at the reference plane. *(Jingye Sun and Attique Dawood contributed equally to this work.)*

REFERENCES

[1] J. Sun and S. Lucyszyn, "Extracting complex dielectric properties from reflection-transmission mode spectroscopy," *IEEE Access*, vol. 6, pp. 8302–8321, 2018.

[2] M. D'Auria, W. J. Otter, J. Hazell, B. T. W. Gillatt, C. Long-Collins, N. M. Ridler, and S. Lucyszyn, "3-D printed metal-pipe rectangular waveguides," *IEEE Trans. Compon., Packag. Manuf. Technol.*, vol. 5, no. 9, pp. 1339–1349, Sep. 2015.

[3] B. T. W. Gillatt, M. D'Auria, W. J. Otter, N. M. Ridler, and S. Lucyszyn, "3-D printed variable phase shifter," *IEEE Microw. Wireless Compon. Lett.*, vol. 26, no. 10, pp. 822–824, Oct. 2016.

[4] W. J. Otter and S. Lucyszyn, "Hybrid 3-D-printing technology for tunable THz applications," *Proc. IEEE*, vol. 105, no. 4, pp. 756–767, Apr. 2017.

[5] W. J. Otter, N. M. Ridler, H. Yasukochi, K. Soeda, K. Konishi, J. Yumoto, M. Kuwata-Gonokami, and S. Lucyszyn, "3D printed 1.1 THz waveguides," *Electron. Lett.*, vol. 53, no. 7, pp. 471–473, Mar. 2017.

[6] *Formfutura Premium ABS—Frosty White*. Accessed: Mar. 07, 2019. [Online]. Available: https://www.formfutura.com/shop/product/premium-abs-frosty-white-275?category=180

[7] G. F. Engen and C. A. Hoer, "Thru-reflect-line: An improved technique for calibrating the dual six-port automatic network analyzer," *IEEE Trans. Microw. Theory Techn.*, vol. MTT-27, no. 12, pp. 987–993, Dec. 1979.

[8] A. Rumiantsev and N. Ridler, "VNA calibration," *IEEE Microw. Mag.*, vol. 9, no. 3, pp. 86–99, Jun. 2008.

[9] N. M. Ridler, "News in RF impedance measurements," in *Proc. 27th Gen. Assem. Int. Union Radio Sci. (URSI)*, Maastricht, The Netherlands, vol. 374, Aug. 2002, pp. 1–4.

[10] N. M. Ridler, "A review of existing national measurement standards for RF and microwave impedance parameters in the UK," in *Proc. IEE Colloq. Microw. Meas., Current Techn. Trends*, Feb. 1999, pp. 6-1–6-6.

[11] *CZ121 Brass*. Accessed: Mar. 07, 2019. [Online]. Available: https://www.metals4u.co.uk/cz121-brass.asp

[12] *Microwave Office Element Catalog, NI AWR Design Environment v13.03*. Accessed: Mar. 07, 2019. [Online]. Available: https://awrcorp.com/download/faq/english/docs/elements/ELEMENTS.htm

[13] R. E. Collin, *Field Theory of Guided Waves*, New York, NY, USA: McGraw-Hill, 1960, pp. 182–195.

[14] S. Lucyszyn, D. Budimir, Q. H. Wang, and I. D. Robertson, "Design of compact monolithic dielectric-filled metal-pipe rectangular waveguides for millimetre-wave applications," *IEE Proc.-Microw., Antennas Propag.*, vol. 143, no. 5, pp. 451–453, Oct. 1996.

[15] K. C. Gupta, R. Garg, and R. Chadha, *Computer-Aided Design of Microwave Circuits*. Norwood, MA, USA: Artech House, 1981.

[16] D. K. Cheng, *Field and Wave Electromagnetics*, 2nd ed. Reading, MA, USA: Addison-Wesley, 1989.

[17] P. I. Deffenbaugh, R. C. Rumpf, and K. H. Church, "Broadband microwave frequency characterization of 3-D printed materials," *IEEE Trans. Compon., Packag., Manuf. Technol.*, vol. 3, no. 12, pp. 2147–2155, Dec. 2013.

[18] *COMSOL RF Module*. Accessed: Mar. 07, 2019. [Online]. Available: https://uk.comsol.com/rf-module

[19] S. Papantonis and S. Lucyszyn, "Lossy spherical cavity resonators for stress-testing arbitrary 3D eigenmode solvers," *Prog. Electromagn. Res.*, vol. 151, pp. 151–167, 2015.

[20] R. Marks and D. F. Williams, "A general waveguide circuit theory," *J. Res. Nat. Inst. Standards Technol.*, vol. 97, no. 5, pp. 533–562, Oct. 1992.

[21] *MATLAB Functions*. Accessed: Mar. 07, 2019. [Online]. Available: https://uk.mathworks.com/help/matlab/functions.html

[22] A. M. Nicolson and G. F. Ross, "Measurement of the intrinsic properties of materials by time-domain techniques," *IEEE Trans. Instrum. Meas.*, vol. IM-19, no. 4, pp. 377–382, Nov. 1970.

[23] W. B. Weir, "Automatic measurement of complex dielectric constant and permeability at microwave frequencies," *Proc. IEEE*, vol. 62, no. 1, pp. 33–36, Jan. 1974.

[24] A.-H. Boughriet, C. Legrand, and A. Chapoton, "Noniterative stable transmission/reflection method for low-loss material complex permittivity determination," *IEEE Trans. Microw. Theory Techn.*, vol. 45, no. 1, pp. 7552–7557, Jan. 1997.

[25] A. N. Vicente, G. M. Dip, and C. Junqueira, "The step by step development of NRW method," in *Proc. SBMO/IEEE MTT-S Int. Microw. Optoelectron. Conf. (IMOC)*, Oct./Nov. 2011, pp. 738–742.

[26] J. J. Barroso and A. L. de Paula, "Retrieval of permittivity and permeability of homogeneous materials from scattering parameters," *J. Electromagn. Waves Appl.*, vol. 24, nos. 11–12, pp. 1563–1574, 2010.

[27] (Mar. 2011). *Highest Available Signal-to-Noise Performance, Delivering Superior Sensitivity and Analytical Performance: Technical Overview*. Accessed: Mar. 07, 2019. [Online]. Available: https://www.agilent.com/cs/library/technicaloverviews/public/si-1353.pdf

[28] IRsweep AG. (2018). *IRis-F1High-Speed Infrared Spectrometer*. Accessed: Mar. 07, 2019. [Online]. Available: http://cloudfront.irsweep.com/resources/IRsweep_IRisF1.pdf

[29] R. Liu, Y. Li, H. Chen, and Z. Wang, "EVM estimation by analyzing transmitter imperfections mathematically and graphically," *Analog Integr. Circuits Signal Process.*, vol. 48, no. 3, pp. 257–262, Sep. 2006.

[30] G. K. Uskov, P. A. Kretov, V. A. Stepkin, N. S. Sbitnev, and A. M. Bobreshov, "Investigation of 3D printed dielectric structure for microwave lens prototyping," in *Proc. 6th Int. Conf. Antenna Theory Techn. (ICATT)*, Kiev, Ukraine, May 2017, pp. 294–296.

[31] R. Guo, E.-M. Stuebling, F. Beltran-Mejia, D. Ulm, T. Kleine-Ostmann, F. Ehrig, and M. Koch, "3D printed terahertz rectangular waveguides of polystyrene and TOPAS: A comparison," *J. Infr., Millim., THz. Waves*, vol. 40, no. 1., pp. 1–4, Jan. 2019.

[32] M. Naftaly, "An international intercomparison of THz time-domain spectrometers," in *Proc. 41st Int. Conf. Infr., Millim., THz. Waves (IRMMW-THz)*, Sep. 2016, pp. 1–2.

[33] L. Oberto, M. Bisi, A. Kazemipour, A. Steiger, T. Kleine-Ostmann, and T. Schrader, "Measurement comparison among time-domain, FTIR and VNA-based spectrometers in the THz frequency range," *Metrologia*, vol. 54, no. 1, pp. 77–84, Jan. 2017.

[34] N. Duangrit, B. Hong, A. D. Burnett, P. Akkaraekthalin, I. D. Robertson, and N. Somjit, "Terahertz dielectric property characterization of photopolymers for additive manufacturing," *IEEE Access*, vol. 7, pp. 12339–12347, 2019.

[35] W. J. Otter and S. Lucyszyn, "3-D printing of microwave components for 21st century applications," in *Proc. IEEE MTT-S Int. Microw. Workshop Adv. Mater. Processes RF THz Appl. (IMWS-AMP)*, Chengdu, China, Jul. 2016, pp. 1–3.

[36] D. M. Pozar, "Transmission lines and waveguides," in *Microwave Engineering*, 3rd ed. New York, NY, USA: Wiley, 2005, pp. 111–119.

[37] *Agilent PNA Microwave Network Analyzers: Data Sheet*. Accessed: Mar. 07, 2019. [Online]. Available: http://literature.cdn.keysight.com/litweb/pdf/5989-7605EN.pdf

JINGYE SUN was born in Changchun, China, in 1989. She received the B.Eng. degree in electronic and electrical engineering from University College London, London, U.K., in 2012, and the M.Sc. and Ph.D. degrees in electrical and electronic engineering from Imperial College London, London, in 2013 and 2018, respectively. She is currently a Visiting Researcher with Imperial College London. Her current research interests include terahertz and thermal infrared technologies, and their applications.

ATTIQUE DAWOOD received the M.S. degree in electrical engineering from the National University of Computer and Emerging Sciences, Islamabad, Pakistan, in 2012. He is currently pursuing the Ph.D. degree in modeling THz resonators at Imperial College London. His current research interests include electromagnetic modeling, THz generators, and coupled resonators in biological systems.

WILLIAM J. OTTER received the M.Eng. degree in electrical and electronic engineering and the Ph.D. degree from Imperial College London, London, U.K., in 2010 and 2015, respectively.

During his M.Eng. degree, he undertook industrial placements with BAE Systems, Advanced Technology Centre, Great Baddow, U.K., and held an IET FUSE Scholarship. Throughout his Ph.D. degree, he held the Val O'Donoghue Scholarship in the Department of Electrical and Electronic Engineering. He was a Postdoctoral Research Associate with Imperial College London, working in the area of millimeter-wave and THz bio-sensors. His research interests include 3-D printing, photonic crystals, low-cost terahertz devices, electromagnetic modeling, optoelectronics, and electromagnetic sensors.

NICK M. RIDLER (M'03–SM'06–F'14) received the B.Sc. degree from King's College London, University of London, London, U.K., in 1981. He is currently the Head of Science with the Electromagnetic and Electrochemical Technologies Department, U.K.'s National Physical Laboratory. He is also a Visiting Professor with the universities of Leeds, Liverpool, and Surrey, U.K., and, a Non-Executive Director of LA Techniques Ltd. He is a Fellow of the Institution of Engineering and Technology (IET) and a Fellow of the Institute of Physics (IOP). He has more than 35 years' of experience working in industrial, government, and academic research establishments. His current research interests include precision high-frequency electromagnetic measurement (from 1 kHz to 1 THz).

Dr. Ridler is the Chair of the IEEE P1785 Standard Working Group for "Waveguides for Millimeter and Sub-Millimeter Wavelengths." He was also Chair of the IEEE MTT Society's "Standards Coordinating Committee" and is a Past President of the Automatic RF Techniques Group (ARFTG). He represents the International Electrotechnical Commission (IEC) on the International Bureau of Weights and Measures (BIPM) Joint Committee for Guides in Metrology (JCGM) Working Group 1 "Expression of Uncertainty in Measurement (GUM)."

STEPAN LUCYSZYN (M'91–SM'04–F'14) received the Ph.D. degree in electronic engineering from King's College London, University of London, London, U.K., in 1992, and the D.Sc. (higher doctorate) degree in millimeter-wave and terahertz electronics from Imperial College London, London, in 2010.

From 1997 to 2012, he taught MMIC Measurement Techniques on IEE/IET short courses hosted by the U.K.'s National Physical Laboratory. He is currently a Professor of millimeter-wave systems and the Director of the Centre for Terahertz Science and Engineering, Imperial College London. He has coauthored over 200 papers and 12 book chapters in applied physics and electronic engineering.

Dr. Lucyszyn served as a Founding Member of the Steering Group for the U.K.'s EPSRC Terahertz Network and a member of the IEEE Technical Committee for Terahertz Technology and Applications (MTT-4). He was a Fellow of the Institution of Electrical Engineers, U.K., and the Institute of Physics, U.K., in 2005. In 2008, he became a Fellow of the Electromagnetics Academy, USA. He was appointed as an IEEE Distinguished Microwave Lecturer, from 2010 to 2013. He is currently a European Microwave Lecturer of the European Microwave Association. He co-founded the Imperial College London spin-out company Drayson Wireless Ltd., in 2014.